I&EC research
Industrial & Engineering Chemistry Research

Article

Cite This: Ind. Eng. Chem. Res. 2019, 58, 9431−9449

pubs.acs.org/IECR

Experimental and Mechanistic Study of Stabilized Dry CO_2 Foam Using Polyelectrolyte Complex Nanoparticles Compatible with Produced Water To Improve Hydraulic Fracturing Performance

Hooman Hosseini,[†] Jyun Syung Tsau,[‡] Karen Shafer-Peltier,[‡] Craig Marshall,[§,∥] Qiang Ye,[⊥] and Reza Barati Ghahfarokhi*[,†]

[†]Department of Chemical and Petroleum Engineering, [‡]Tertiary Oil Recovery Program, [§]Department of Geology, [∥]Department of Chemistry, and [⊥]Institute for Bioengineering Research, University of Kansas, Lawrence, Kansas 66045, United States

Supporting Information

ABSTRACT: The amount of fresh water used in hydraulic fracturing can be significantly reduced by employing produced water-compatible supercritical CO_2 ($scCO_2$) foams. Foams generated using surfactants only have suffered from long-term stability issues resulting in low viscosity and proppant-carrying problems. In this work, foam lamella stabilization with polyelectrolyte complex nanoparticles (PECNPs) and wormlike micelles (WLMs) is investigated. Electrostatic interactions are studied as the defining factors improving the hydraulic fracturing performance using the PECNP system prepared in produced water. Two oppositely charged polyelectrolytes are investigated to generate a more stable lamellae between the aqueous phase and the $scCO_2$ while degrading in the presence of crude oil. The generated dry foam system is used as a hydraulic fracturing fluid in a tight shale formation. The strong compatibility of the synthesized PECNPs with zwitterionic surfactants prepared in highly concentrated brine in the form of wormlike micelles above critical micelle concentration (CMC) helps develop a highly viscous, dry foam capable of using produced water as its external phase. This foam system improves fracture propagation and proppant transport fracture cleanup compared to the base case foam system with no PECNPs. The formation of PEC−surfactant nanoparticles was verified via zeta potential, particle size analysis, and transmission electron microscopy; the underlying mechanism was identified as electrostatic rearrangement of WLMs along the PECNP's perimeter or formation of electrostatically bonded micelles with the nanoparticle to create a new enhanced nanoparticle. A Raman spectroscopic model was developed to understand the PECNP−surfactant spectra and subsequent spectroscopic and hence structural changes associated with complexation. Enhanced bulk viscosity and improved foam quality as a result of complexation at the interface was identified with rheometry in addition to sand pack experiments with PECNP−surfactant ratios of 1:9 and 4:6 in 33.3 kppm and 66.7 kppm salinity brine systems, respectively. Enhancement in the shear thinning and cleanup efficiency of the fracturing fluid was observed. Formation damage was controlled by the newly introduced mixtures as fluid loss volume decreased across the tight Kentucky sandstone cores by up to 78% and 35% for $scCO_2$ foams made with PECNP−WLMs in 33.3 and 66.7 kppm salinity brine, respectively. The produced water compatibility and reduction of water disposal presented the prospect of environmentally friendly $scCO_2$ foams for hydraulic fracturing of unconventional reservoirs.

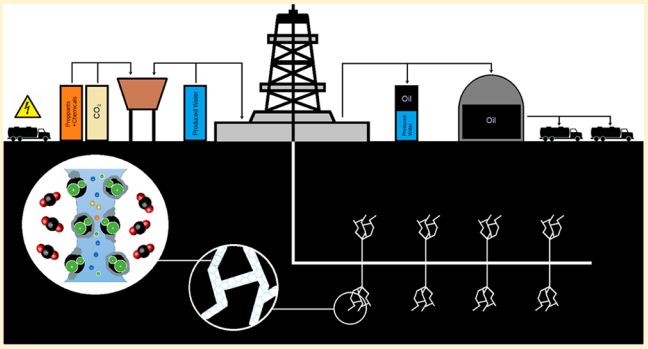

1. INTRODUCTION

Unconventional oil and gas resources are under increasing demand because of the rapid climb in energy consumption, technological advances, and depletion of easy-to-produce conventional resources. Prospects of unconventional technologies such as hydraulic fracturing and directional drilling represent a future energy portfolio and a game-changing production technique that outperforms conventional drilling methods to stimulate shale and tight hydrocarbon reservoirs.[1,2] First introduced into commercial practice in 1947 and effectively combined with horizontal drilling in the late 1990s, hydraulic fracturing is the most enduring technology ever developed to enhance gas and petroleum liquid production from low-permeability formations (permeability less than 1 mD and below 15% porosity).[2−4] Upon fracture creation, the pressurized fluid carrying the proppant is injected to the fractured reservoir to keep the fracture propped open and to let the hydrocarbons flow from the fractures to the producing well and surface.[5] Hydraulically fractured oil and gas

Received: March 12, 2019
Revised: May 8, 2019
Accepted: May 8, 2019
Published: May 8, 2019

DOI: 10.1021/acs.iecr.9b01390
Ind. Eng. Chem. Res. 2019, 58, 9431−9449

Table 1. Mississippian Limestone Play Brine Composition (Original and Laboratory Concentrations)

MLP		elements						
		Ca	Mg	Na	K	Cl	Sr, Fe, Mn, SO_4, etc.	total
nominal concentration	concentration (mg/L)	12 780.4	2 601.1	64 779.4	374.9	120 630	1 482.6	202 648.4
synthesized MLP	salt	NaCl	Na_2SO_4	KCl	$MgCl_2{\cdot}6H_2O$	$SrCl_2{\cdot}6H_2O$	$CaCl_2{\cdot}2H_2O$	total
lab concentration	concentration (mg/L)	163 661	1 224	715	21 759	1 535	46 886	235 780

wells are typically located near drinking water resources; thus, the water cycle process could influence the quality of drinking water in different stages, from water withdrawal and chemical mixing of fracturing fluids to water disposal and reuse of produced water.[6] The impact could have negative consequences on areas of lower water availability, in terms of groundwater and surface water quality,[7] spill management,[8] fracturing pad leakage,[9] high cost of water disposal,[4] excessive water withdrawal, and water contamination.[6] As large amount of fresh water, groundwater, or surface water (about 5.7 million L between 2011 and 2013[6]) are used for hydraulic fracturing, a water management strategy within the fracturing process can reduce the frequency of severity of impacts on earthquakes and drinking water and expenses associated with water treatment.

Low initial water saturation in the majority of tight shales makes water blocking, caused by injection of water-based fluids, a more effective mechanism in decreasing permeability.[10,11] Water trap due to capillary retention,[10] costly pressure drawdown to recover the water,[12] and abundance of water-sensitive formations[13] highlight the importance of waterless fracturing techniques that are capable of carrying proppants[4] while maintaining the fracture conductivity using the least amount of water.

The development of "water-less" fracturing fluids in the form of foams containing stabilizers such as nanoparticle and surfactants introduces a viable solution for water-sensitive formations.[14] Foams, as a predominant dispersion of gas in liquids, are promising candidates to address the issue with variable amounts of water and at least one compressible component, such as CO_2 or N_2, within the composition.[3] CO_2 is abundant, nonflammable, and nontoxic, and CO_2 emission into the atmosphere prompts the efforts for effective capture utilization and storage (CCUS).[15,16] The low density and viscosity of CO_2 enhance the propagation in low-permeability reservoirs; however, there exist issues reported with ice formation[17] and challenges in storage[18] and filtration of liquid CO_2-based fracturing fluid.[4] CO_2 storage in the dense phase is performed in the supercritical state where the fluid is held above the critical point (31.1 °C and 7.4 MPa).[19] $scCO_2$ offers properties such as enhanced rates, improved mass transfer, and increased selectivity[20] between the CO_2 gas (diffusivity) and CO_2 liquid (density), indicating a prime candidate for fracturing.[21,22]

To enhance the compatibility of $scCO_2$ with the water phase, a variety of methods have been proposed. The presence of adsorbed surfactant layers stabilizes the lamellae between the $scCO_2$ and the aqueous phase,[23] taking advantage of electrostatic repulsion between the two faces of the lamellae.[24] Likewise, increasing the surfactant concentration under the influence of electrolyte concentration would help with formation of a long-range electrostatically ordered microstructure on the thin liquid films and the bulk of the lamellae to inhibit foam film drainage (stratification).[25] Formation of viscoelastic lamella stabilizes the gas-in-water foams by suppressing the gravity drainage, lamella thinning, and eventually Ostwald ripening.[22]

Nanoparticles[5] were found to overcome the challenges associated with surfactant adsorption on reservoir rocks,[4] thermal conductivity,[26] fluid loss,[27] water invasion,[28] fluid propagation in porous media,[5,29] and pore throat plugging[30] to achieve proper fracture width and height.[4] Polyelectrolytes are widely used charged polymers compatible with aqueous solutions while being useful for adsorption,[31] ionic conduction,[32] ultrafiltration,[33] and controlled release.[34] Branched polyethylenimine (PEI) with different types of cationic amine functionality is capable of polyelectrolyte complex nanoparticle (PECNP) formation in electrostatic complexation with dextran sulfate (DS) comprising anionic sulfonate functionality in an adjusted pH medium.[3] In this work, electrostatic interaction between polyelectrolyte complex nanoparticles with entangled wormlike micelles (WLMs) of a viscoelastic surfactant (VES) is investigated to eliminate fluid loss issues, to improve the viscosity of VES-based fluids, and to enhance the proppant suspension capabilities. To understand the underlying mechanism of synergistic electrostatistic complexation between surfactant and polymer in the bulk lamella mixture, Raman spectroscopy was employed. In order to tailor ionic activity of surfactants and to decrease the rate of lamellae drainage, polyelectrolyte complex nanoparticles were developed by our group for both enhanced oil recovery (EOR), reservoir treatment, and hydraulic fracturing applications.[3,34−38] Interactions between the polyelectrolytes and oppositely charged sites on the surfactant create a variety of different colloidal systems with liquid crystalline-like mesostructured and long-range order on nanometer scale. The supercharged and stable nano aggregates in high-salinity produced water are capable of stabilizing the CO_2−water interface to resist against the shear around the wellbore, to carry the proppants to the fracture, and to reduce leak-off in tight formations. The stability of optimized proportions of PECNP−surfactant in high-salinity brine improves the viscosity, elasticity, and fracture conductivity, whereas rapid oil instability is offered through oil spreading through the lamella.

2. MATERIALS AND METHODS

2.1. Material Synthesis and Preparation. High-salinity brine was synthesized according to the procedure introduced by Hosseini et al.[3] The Mississippian limestone play (MLP) recipe contains aqueous solution of more than 202 848 ppm total dissolved solids consisting of $CaCl_2{\cdot}2H_2O$ (Fisher Chemical, certified ACS), $MgCl_2{\cdot}6H_2O$ (Fisher Chemical, certified ACS, crystalline), $SrCl_2{\cdot}6H_2O$ (Fisher Science Education, lab grade), Na_2SO_4 (Fisher Chemical, certified ACS, granular) NaCl (Fisher Chemical, certified ACS, crystalline), and KCl (Fisher Chemical, potassium chloride for calomel cells, crystalline). The salts were added to reverse osmosis and deionized water (RO- DI- water). The salt type and concentration in MLP brine are shown in Table 1. The

DOI: 10.1021/acs.iecr.9b01390
Ind. Eng. Chem. Res. 2019, 58, 9431−9449

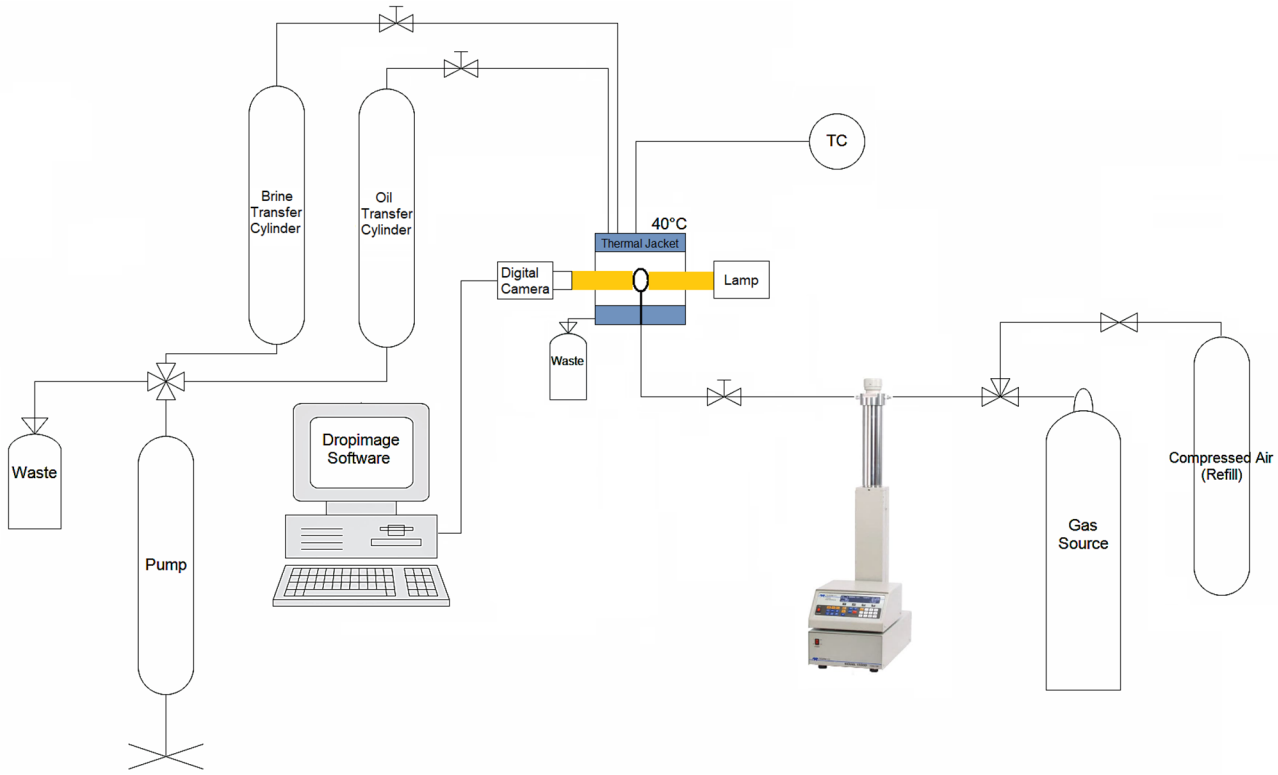

Figure 1. Process flow diagram for interfacial tension analysis setup.

highly concentrated brine synthesized according to the laboratory recipe adopted from the original MLP recipe (202 848 to ~200 000 ppm) was then diluted to 66 666 ppm (3×) and seawater level 33 333 ppm (6×) nominal concentrations.

Zwitterionic surfactant HDP-0761-12-2AM was provided by Harcros Chemicals Inc. The surfactant structure was designed for optimum ionic activity in the form of short-chain aliphatic molecules with positive amine and negative sulfonate functional groups. The main ingredients in the form of solvent and additive to the surfactant solutions are listed in Table S1.

The surfactant was dissolved in 33.3 and 66.7 kppm brines to form 1 w/w % reference solutions. Polyelectrolyte complex nanoparticles (PECNP) were prepared according to the procedure developed by Barati and co-workers.[3,36,37] Branched polyethylenimine (PEI) was obtained from Sigma-Aldrich with an average molecular weight of 25 000 g/mol, 1.03 g/mL density at 25 °C, and corresponding viscosity ranging between 13 000 and 18 000 cP at 50 °C. DS was provided from Sigma-Aldrich with 500 000 g/mol molecular weight. PEI and DS were separately dissolved in high-salinity brines with 1 w/w %, and the pH for the PEI solution was lowered to 8.5 by addition of 6 N HCl[3,37] (Figure S1 in the Supporting Information). The solution of 1 w/w % DS in high-salinity brine was prepared, and PEI and DS solutions were mixed accordingly. The mixing ratio of PEI to DS to the diluting brine solution (PEI:DS:brine) was chosen to be 3:1:0.1 to make positively charged nanoparticles. This ratio was developed based on previous observations with zeta potential and particle size measurements.[35,36] The nanoparticle solution was mixed with surfactant solutions (1 w/w %) in both 33.3 kppm and 66.7 kppm brine systems for 20 min to form the PECNP/surfactant complexation with different mixing ratios of PECNP:surfactant (1:9, 2:8, 3:7, and 4:6). The concentration of the surfactant remains constant in mixing with nanoparticles (1 w/w %). The foaming solution was later mixed with air (50 v/v %) or $scCO_2$ (90 v/v %) in inline mixers at 40 °C to form the actual foam.

2.2. Fourier Transform-Infrared (FT-IR) Spectroscopy. The chemical functional groups on the surfactant molecules were examined with a Spectrum 400 FT-IR spectrometer (PerkinElmer, Waltham, MA) equipped with two temperature-stabilized deuterated triglycine sulfate detectors. A small aliquot of liquid sample was deposited onto the diamond crystal top plate of an attenuated total reflection (ATR) accessory (GladiATR, Pike Technologies, Madision, WI). Sixty scans were coadded over the range of 4000−650 cm^{-1} with a spectral resolution of 4 cm^{-1}. Air was taken as the reference for the background before each sample. After acquisition of each spectrum, the ATR plate was cleaned in situ by ethanol solution three times and allowing it to dry. No residue from the previous sample was observed in subsequent background spectra and when compared to the previous background spectra. In addition, an atmospheric correction routine was performed for CO_2/H_2O suppression by the Spectrum software (PerkinElmer, Waltham, MA). The results are shown in Figure S2.

2.3. Dynamic Light Scattering. The hydrodynamic diameter of ionic particles was measured by dynamic light-scattering measurement, through the average of three readings using a NanoBrook Omni particle sizer and zeta potential analyzer by Brookhaven Instruments. The pH of colloidal solutions, density and viscosity of each sample, and mean particle diameter were employed for determining the zeta potential. For the zeta potential measurements, the samples were diluted 20 times in background electrolyte of 1 mM KCl, where the average of three readings were considered for

DOI: 10.1021/acs.iecr.9b01390
Ind. Eng. Chem. Res. 2019, 58, 9431−9449

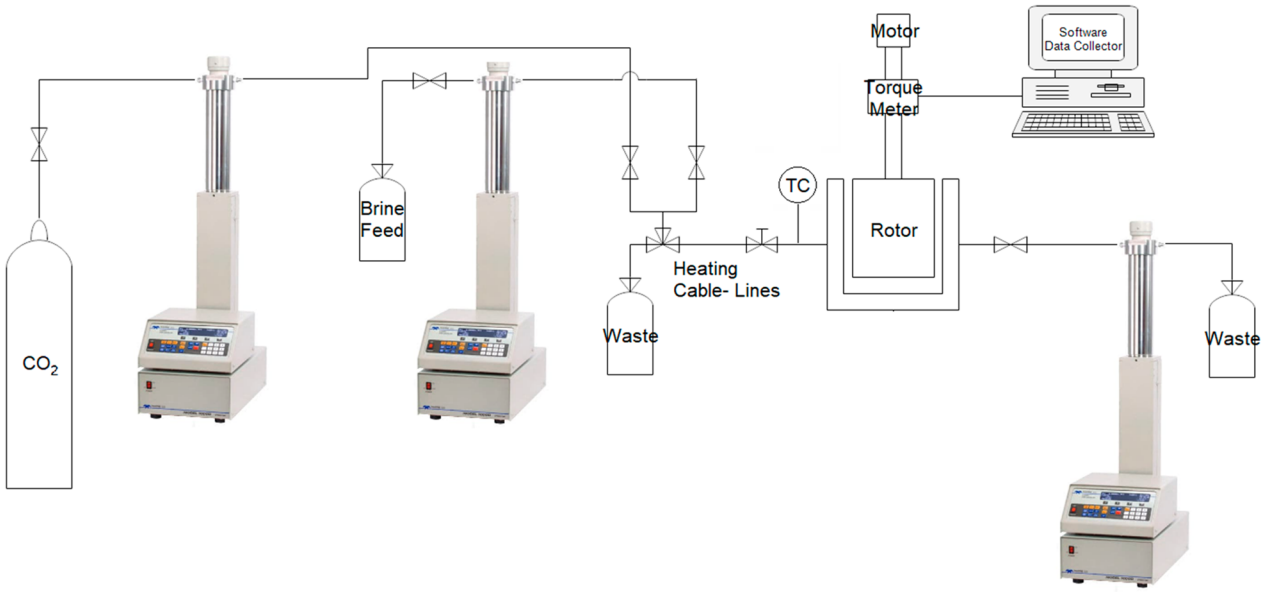

Figure 2. Process flow diagram for rheometer setup.

analysis on the NanoBrook Omni. The standard 35 mV red diode laser with nominal 640 nm wavelength was employed to detect the size range, size distribution, and electrophoretic mobility using the Smoluchowski model.

2.4. Air Foam Stability Measurements. The experimental setup was designed to quantify bulk foam height as a function of time to determine the aqueous foam stability. The predetermined amount (10 mL) of foaming solution comprising different proportions of PECNP to surfactant (PECNP:surfactant of 1:9, 2:8, and 3:7) was transferred to 20 mL vials for primary foam decay analysis. The sealed and scaled vial containing the 50% mixture with air was heavily agitated almost 30 times for perfect mixing of air and liquid. The scaled vial was placed and kept in an oven with a constant temperature of 40 °C (Figure S3). A camera was set inside the oven, and the air foam height in the vials was recorded every minute.

2.5. Interfacial Tension Analysis. The $scCO_2$ interfacial tension in high-salinity brine containing surfactants and PECNP was measured according to the axisymmetric drop shape analysis of pendant drop by a tensiometer at pressures and temperatures in which CO_2 is in supercritical conditions. The $scCO_2$ bubble is formed on the tip of a stainless steel capillary in a high-pressure chamber (1330 psi) filled with PECNP−surfactant solution while the isothermal temperature of 40 °C was maintained by applying thermal jackets around the pipes and chamber. The DROPimage software and high-resolution camera were employed to measure the surface tension for each bubble in dynamic mode for 1 h. A minimum of three runs for each sample was recorded. A schematic of the employed tensiometer in this analysis is provided in Figure 1. The droplet area was determined by analyzing the droplet profile using a camera coupled with image analyzer software (DROPimage).

The critical micelle concentration (CMC) was determined with different concentrations of surfactant dissolved in high-salinity brines, and the corresponding interfacial tension was estimated accordingly. Dilatational elasticity was estimated according to a ramp-type perturbation approach previously presented by Tewes and co-workers.[39] The variation of interfacial pressure after compression of the equilibrated surface layer of pendant drop ($\Delta\pi_e$) is correlated to surface area variation $\left(\frac{\Delta A}{A_i} = \frac{U_b t}{A_i}\right)$ as a result of mechanical strain to estimate the equilibrium surface dilatational elasticity:[39,40]

$$\Delta\pi_e = E_e \frac{U_b t}{A_i} \tag{1}$$

where A_i is surface area prior to applying the mechanical strain, U_b the constant velocity of compression during the time (t), and E_e the equilibrium surface dilatational elasticity. The nonequilibrium portion of surface pressure variation ($\Delta\pi_{ne}$) is also calculated based upon dissipation of accumulated energy during compression and relaxation,[39] where τ stands for relaxation time.

$$\Delta\pi_{ne} = \frac{E_{ne} U_b t}{A_i}(1 - e^{-t/\tau}) \tag{2}$$

Details of the calculations are presented in the Supporting Information (Figure S4).

2.6. Rheological Measurements. The oscillatory shear stability of bulk foam is examined through stress-controlled rotational measurements using an Anton-Paar MCR 302 rheometer. The temperature was controlled by a water-circulating bath (6−40 °C). The setup utilized feed cylinders, pumps, circulating coolers, and thermal isolators (Figure 2). A Couette geometry module was used in a pressure cell to study the viscoelastic behavior of $scCO_2$ foam. Constant (2000 s^{-1}) and variable shear rates (2000−100 s^{-1}) were used for static (stagnant foam in the cell) and dynamic (continues flow of foam in the cell) measurements at 40 °C and 1350 psi. The detailed procedure is introduced in the Supporting Information.

2.7. Raman Spectroscopy. Raman spectra of lyophilized powders were determined by using a LabRAM ARAMIS Raman spectrometer (LabRAM HORIBA Jobin Yvon, Edison, NJ) with a HeNe laser (λ = 633 nm, power = 17 mW) as an excitation source. The instrument conditions were 200 μm

DOI: 10.1021/acs.iecr.9b01390
Ind. Eng. Chem. Res. 2019, 58, 9431−9449

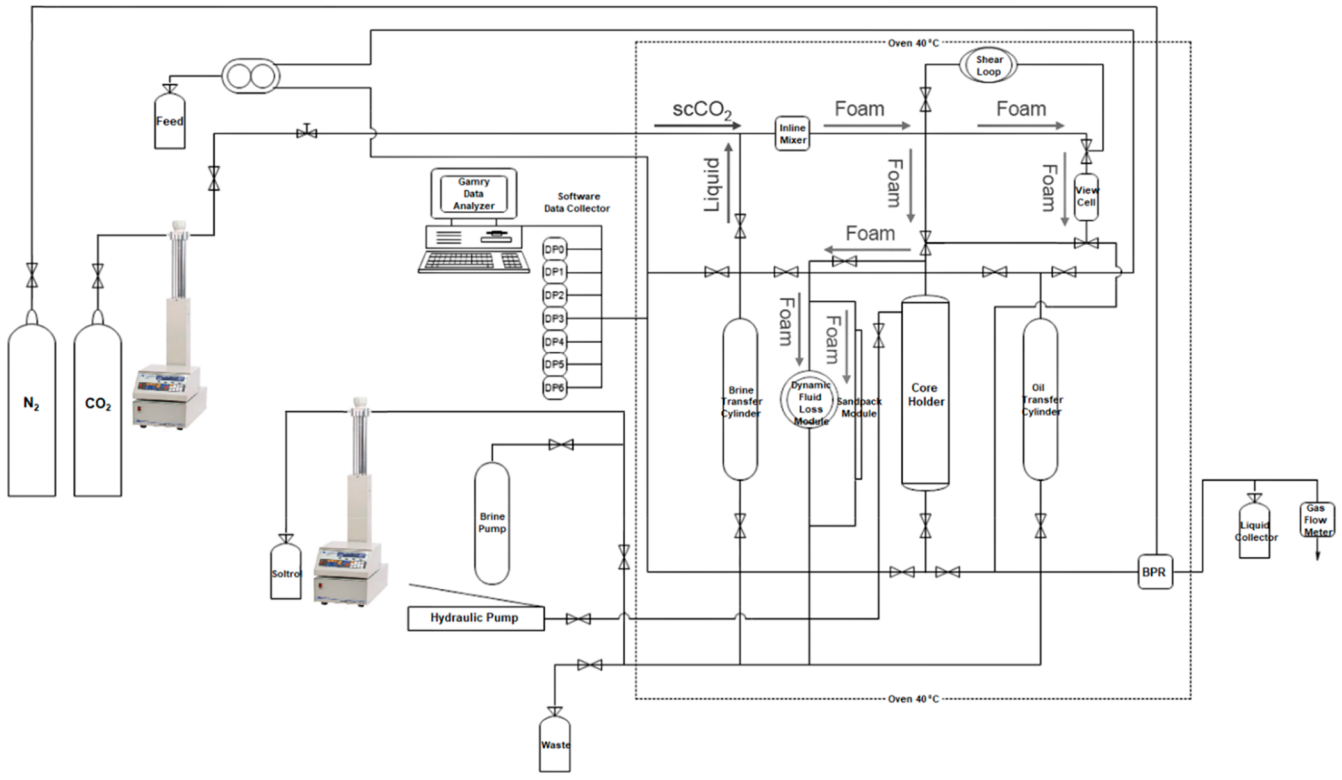

Figure 3. Flow diagram for high-pressure−high-temperature CO_2 foam flooding setup with view cell foam stability module, fluid loss, and sand pack modules. Pathways A, B, and C represent the foam flow through view cell, dynamic fluid loss, and sand pack modules.

confocal hole, 150 μm wide entrance slit, 600 g/mm grating, and 50× long working distance objective Olympus lens. Data acquisition was performed using LabSPEC 5 (HORIBA Jobin Yvon). The samples were mounted in a computer-controlled, high-precision $x-y$ stage. Spectra were acquired over a range of 700−2400 cm^{-1} with 60 s exposure time and 10 times accumulation.

The acquired Raman spectra were processed using Matlab (the MathWorks, Inc., Natick, MA) to smooth the curves (through binning adjacent data points), to remove digital noise (through binning adjacent data points), and to remove the fluorescence background (by subtracting a fifth-order polynomial fit to the original spectrum). Furthermore, contributions to the spectra from cosmic rays were removed manually when appropriate. The spectra of mixtures of PECNP and surfactant (1:9 ratio) were fit with average surfactant and PECNP spectra using least-squares fitting in a manner similar to the method described by Shafer-Peltier et al. for modeling of biological Raman spectra.[41]

Spectra of dextran sulfate and polyethylenimine were also collected in the same manner to aid in data interpretation and peak assignment but were not included in the model. Vectors representing each fit were created using the MATLAB polyval function, and residuals of each fit were determined. An average of three to four spectra were then used (except in the case of the PECNP:surfactant complex spectra) for further analysis.

2.8. Transmission Electron Microscopy (TEM). The 5 μL samples of solutions of PECNP and PECNP−surfactant mixture were placed onto a 300 mesh Lacey carbon copper grid (EMS LC 300 Cu), separately, for 1 min and blotted twice with a filter paper. The 300 mesh copper grids with PECNP and PECNP−surfactant mixture were examined using a 200 kV FEI Tecnai F20 XT field emission transmission electron microscope at an electron acceleration voltage of 160 kV. TEM images were captured using a normative and standardized electron dose on an eucentric specimen stage and a constant defocus value from the carbon-coated surfaces. Images were randomly acquired in a size of (1024 × 1024) pixel resolution at 10 different locations within the grid.

2.9. View Cell, Dynamic Fluid Loss, and Sand Pack Measurements. The $scCO_2$ foam stability, core fluid loss properties, and fracture clean up performance were examined via a high-pressure−high-temperature foam flooding apparatus utilized with shear loop mixer, sapphire view cell, dynamic fluid loss, and sand pack modules. The schematic of the system is presented in Figure 3.

The foam is generated with in-line mixing of $scCO_2$ foam (40 °C, 1350 psi) and the aqueous solution (surfactant or PECNP:surfactant solutions) prepared in 33.3 and 66.7 kppm high-salinity brine with different proportions of PECNP:surfactant (1:9, 2:8, 3:7, and 6:4, with 0:10 being the surfactant solution itself). The foaming liquid is mixed with $scCO_2$, and the components are directed toward the Swagelok inline mixer with 7 μm pore size. The generated foam is then directed to the view cell to measure the foam stability and foam textural properties. A GoPro camera was set to record the foam height every minute, and a HAYEAR camera microscope was used to observe the foam microstructure. After the foam was established in the view cell, oil was immediately introduced to the view cell to evaluate the stability of the $scCO_2$ foam in the presence of crude oil. The generated foam could also be directed to the fluid loss module embedded with a low permeability Kentucky sandstone (Table 2) sitting perpendic-

DOI: 10.1021/acs.iecr.9b01390
Ind. Eng. Chem. Res. 2019, 58, 9431−9449

ular to fluid flow to measure the ability of fracturing fluid to prevent the leak-off in the tight formation.

Table 2. Physical Properties for Kentucky Sandstone Core[a]

core	gas permeability	brine permeability	porosity	UCS strength
Kentucky sandstone core	1−5 mD	0.18 mD	14%	8000 psi

[a]Data Provided by Kocurek Industries. Reprinted with permission from ref 3. Copyright 2018 SPE.

The volumes of lost gas and liquid through the core and their corresponding fluid loss coefficients were measured according to the following equation[42]

$$V_L = C_w\sqrt{t} + S_P \quad (3)$$

where V_L is the total fluid loss volume (gas and liquid), C_w the fluid loss coefficient (wall-building coefficient), and S_p the volume leaked off before any filtration occurred.

The mixture of $scCO_2$ and foaming solution can also be directed to a pack of low-density, 20/40 mesh size, ceramic proppant (CARBOECONOPROP provided by Carbo Ceramics Inc.)[43] saturated with high-salinity brine (predetermined pore volume) and MLP crude oil. The sequence for the sand pack experiment includes primary brine flood to measure the initial pack permeability, oil flood for pack saturation, foam flood for pack cleanup, and secondary brine flood for final pack permeability after cleanup. The pressure difference across the dynamic fluid loss and sand pack is monitored with Validyne pressure transducers linked to a Gamry data analyzer. The system contains the left transfer cylinder filled with foaming solution and right transfer cylinder filled with MLP crude oil with the properties provided in Table 3.

Table 3. MLP Crude Oil Properties

oil	viscosity (40 °C, 750 s^{-1})	density
Mississippian crude oil	3.88 cP	0.83 g/cm^3

3. RESULTS

3.1. Particle Size and Zeta Potential Measurements. The particle size and zeta potential values for a variety of PECNP:surfactant proportions (1:9, 2:8, 3:7, and 4:6) in 33.3 and 66.7 kppm brine solutions are presented in Figure 4.

For the 33.3 kppm brine system, PEI and DS form PECNPs within the size range of 132−140 nm with an average zeta potential of +16 mV (Figure 4a,c) because of an excess of amine functional groups on the outer layer of the nanoaggregates resulting in a positive charge (PEI:DS 3:1). Addition of nanoparticles with the lowest proportion (1:9) to the surfactant solution enhances the average particulate size, preventing the fluid loss of the final mixture by bridging the pores on the surface of the rock matrix.[44] Nevertheless, further addition of PECNP lowers the average particle size because of precipitation and charge instability[45,46] (Figure 4a). Accordingly, PECNP:surfactant with the 1:9, 2:8, and 3:7 ratios represent the highest positive zeta potential on the surface of nanoaggregates, and no further stable charge accumulations were observed for higher proportion of PECNP in the 33.3 kppm brine system because of ionic and charge imbalances on the PECNP and surfactant coagulates, allowing electrostatic attractions of opposite charges and electrostatic instabilities. Considering the combined effect of particle size and charges, the 1:9 and 2:8 ratios for PECNP:surfactant are the prime candidates to stabilize the CO_2−water lamella and prevent the fluid loss in 33.3 kppm brine mixtures.

Particle size and potential for ionic mixtures in the 66.7 kppm system are represented in Figure 4b,d. Addition of PECNP to WLMs directly enhances the particle size and positive potential. Higher salinity enhances the hydrophilicity of formed nanoparticles, and it accelerates the aggregation of PECNPs, and PECNP−surfactant because of weakening of electrostatic repulsions and higher concentration of divalent ions.[47] As previously reported, the stronger adsorption of nanoparticles on the lamellae and formation of an electrostatic dense layer in the lamella results in particles with larger zeta potentials;[30,48] therefore, ratios of 3:7 and 4:6 result in optimal size and surface charge in the 66.7 kppm high-salinity brine, and the stable quasi colloidal particles of PECNP and surfactants (WLMs) can withstand the harsh conditions of high-salinity brine.

3.2. Foam Stability Measurement. For the initial stage of stability measurements (Figure S5), the foaming mixture was mixed with air. The foam height was measured with respect to time. Zhang and co-workers reported adsorption and self-assembly of micelles above CMC at the air−water interface for ionic surfactants forming surface segregation with hydrophobic and hydrophilic regions thus repartitioning around the gas−liquid interface.[49] The surfactant−water solubility and nanoparticle compatibility to the ionic interface helped to create relative stability as the resulting foam remains stable for at least 100 min when optimum concentrations of micelles and nanoparticles exist.

Actual foam stability measurements were performed on the $scCO_2$ mixture with PECNP−surfactant in high-salinity brines. Figure 5 illustrates the foam stability measurements and the actual foam formation and degradation inside the sapphire view cell (Figure 5c). Fine-textured and homogeneous cellular structures with dominant microcellular texture (∼200−300 μm) were formed with different ratios of PECNP-to-surfactant solutions. Uniform bubble size and distribution was achieved with 1:9 and 4:6 portions of PECNP to surfactant (Figure 5d).

Likewise, the longest-lived foam belongs to 1:9 and 4:6 ratios in the 33.3 and 66.7 kppm brines, respectively, as foam preserves the cellular structure for at least 2 h in the view cell in these scenarios. The foam half-decay times for different systems are presented in Table 4. The half-decay time for PECNP−surfactant (with 1:9 ratio in 33.3 kppm brine) is more than twice that of 1 wt % surfactant mixed with $scCO_2$. The half-life shortens when a higher portion of nanoparticle is used because of lower electrostatic repulsions, as explained in section 3.1. In contrast, for 66.7 kppm brines, a higher proportion of nanoparticle to surfactant increases the half-life dramatically (PECNP:surfactant 4:6 in 66.7 kppm). Recently, Al-Anssari and co-workers reported that the increased surface tension caused by increasing salinity can eliminate the stabilizing influence of nanoparticles at the CO_2−brine interface.[50]

Bubble rupture and CO_2−water lamella drainage occur in a longer period with lower rate, when PECNP forms ionic complexes with WLMs resulting in stronger electrostatic interactions in the lamella, including the plateau border and lamella border wall. In 66.7 kppm salinity brine, addition of PECNP to surfactant deteriorates the foam stability to some

DOI: 10.1021/acs.iecr.9b01390
Ind. Eng. Chem. Res. 2019, 58, 9431−9449

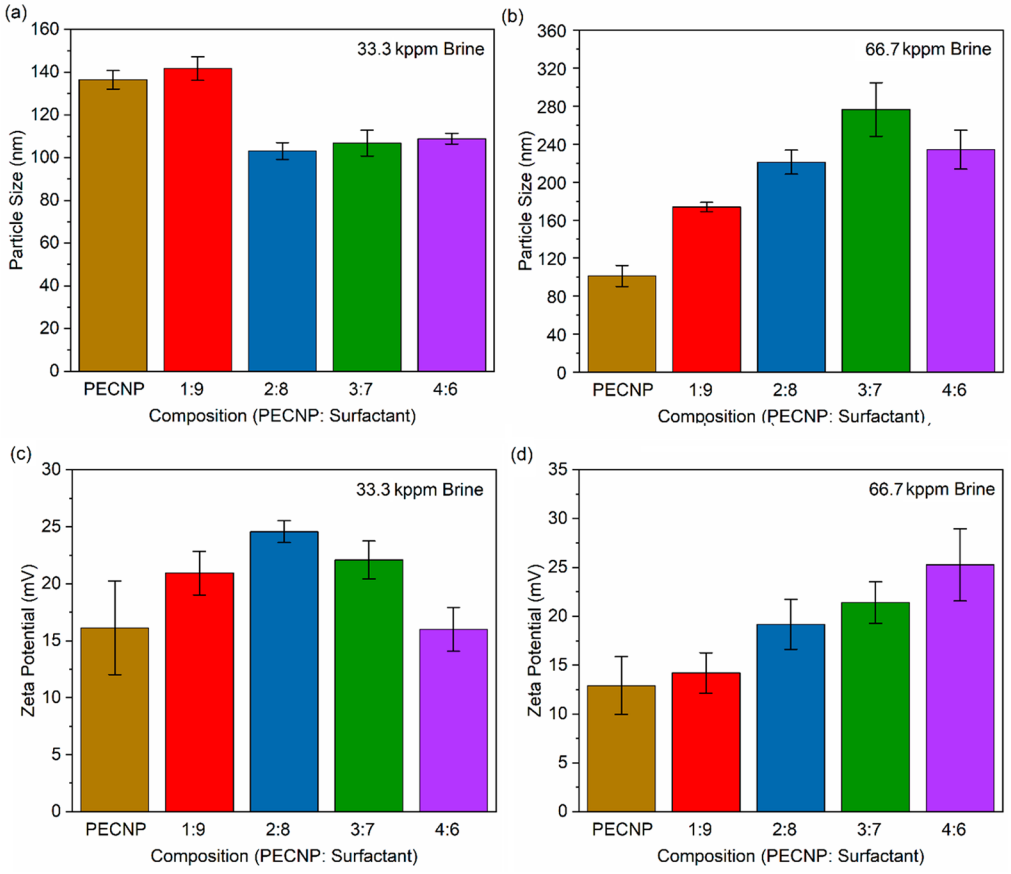

Figure 4. Particle size and zeta potential measurements for PECNP and different proportions of PECNP to surfactant in 33.3 and 66.6 kppm brine systems.

extent because of excessive charge attractions destabilizing the lamella (section 3.1). However, increasing the PECNP–surfactant solution ratio (to PECNP of around 40 v/v %) provides a very stable lamella against lamella drainage, bubble coalescence, and coarsening.

In foam fracturing, the initial good film stability at initial stages is necessary; however, the generated foam needs to degrade when it comes in contact with oil, breaking, as fast during the flow back, leaving behind a fracture with high effective conductivity.[3] Therefore, an unstable lamella is required upon introduction of oil to a foaming system. The foam stability measurements in the presence of oil are shown in Figure 6, where $scCO_2$ foam made in 33.3 and 66.7 kppm was exposed to MLP crude oil in a view cell, and the foam height with respect to time is shown. The most stable foams presented in Figure 5 (with 1:9 and 4:6 PECNP:surfactant ratios) are the least stable ones with fastest drainage when the oil is introduced to the view cell (Figure 6a,b).

As was previously noted, because of low interfacial tension between CO_2 and oil at high pressures, crude oil enters the original lamella, spreading and accelerating the thinning of lamella, coarsening the foam, and causing gas bubble coalescence.[51,52] The time frame of the lamella breakage depends heavily on the interaction of oil with the chemical components residing in the lamella, in this case, the PECNP–surfactant complexes in lamella. As WLMs meet the oil molecules, the oil collapses into an emulsion.[25] The PECNP is also susceptible to degradation as carboxylic acid groups on MLP crude oil can trigger the secession of coiled PEI-DS chains and electrostatic desorption of amine functional groups, resulting in instability of the PECNP–WLMs in the lamella. Configuration of the oil at the gas–aqueous interface is another determining factor in oil instability, when the pseudoemulsion film formed between the oil and the gas is ruptured and oil spreads at the interface (bridge configuration).[40] Accordingly, disintegration of the interface is anticipated because of positive entering and spreading coefficients previously reported by Xiao et al.[53] Table 5 summarizes the entering (E) and spreading (S) coefficients obtained by interfacial tension measurements using the underlying equations for calculation as follows:[54]

$$E = \sigma_{wg} + \sigma_{ow} - \sigma_{og} \quad (4)$$

$$S = \sigma_{wg} - \sigma_{ow} - \sigma_{og} \quad (5)$$

Surface tension between the oil and $scCO_2$ (σ_{og}) is considered a negligible value, because the operating condition is above the minimum miscibility pressure (MMP) of the MLP and $scCO_2$ (MMP $\approx$ 1200 psi). Considering the positive values of E and S, crude oil is capable of entering the gas–water interface and spreading on the liquid lamella; therefore, the weakening of the disjoining pressure by disturbing the PECNP–surfactant charge distribution and desorption to the lamella occurs spontaneously.[53]

3.3. Bulk Rheological Properties. Hydraulic fracturing fluids experience high shear rates because fluid flows through the wellbore tubular and the shear rate drops significantly as the fluid gets into the fracture.[25] Therefore, shear rate sweep

DOI: 10.1021/acs.iecr.9b01390
Ind. Eng. Chem. Res. 2019, 58, 9431–9449

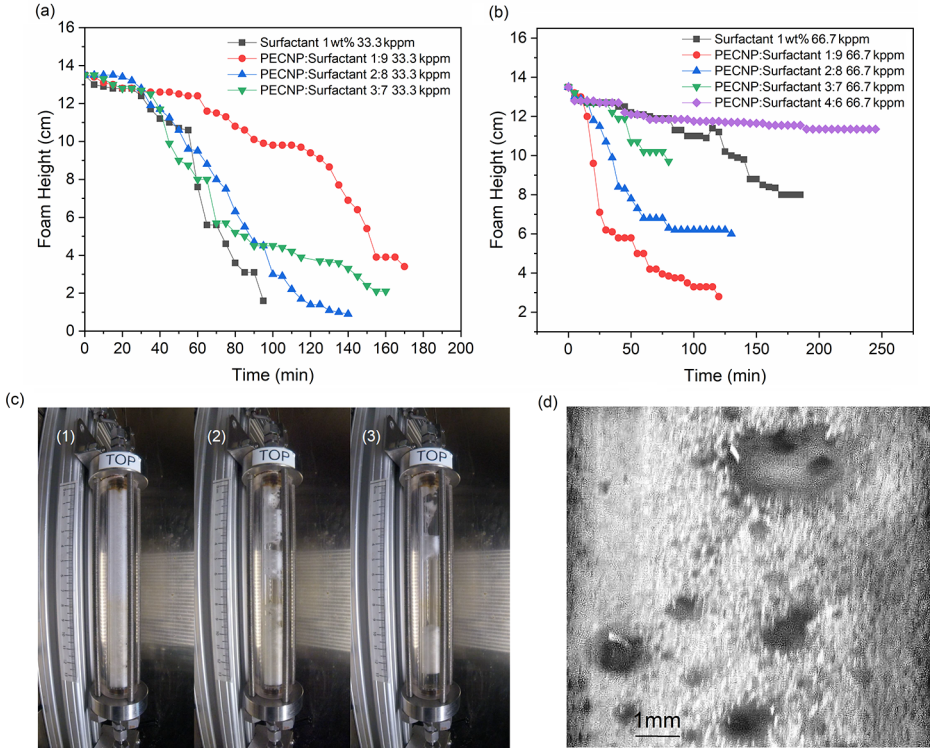

Figure 5. Foam stability measurements for $scCO_2$ foam made with a variety of PECNP−surfactant mixtures in (a) 33.3 kppm brine solutions and (b) 66.7 kppm brine solutions. (c-1) Foam generation and isolation in the view cell; (c-2) foam drainage progress; (c-3) total foam disappearance and breakage. (d) Foam microstructural view inside the view cell for PECNP:surfactant 1:9 in 33.3 kppm brine. Panels a and b are reprinted with permission from ref 3. Copyright SPE 2018.

Table 4. Foam Half Decay Time for a Variety of PECNP−Surfactant Proportions[a]

33.3 kppm of system	half decay time (min)
surfactant-$scCO_2$	65
PECNP:surfactant-$scCO_2$ (3:7)	70
PECNP:surfactant-$scCO_2$ (2:8)	80
PECNP:surfactant-$scCO_2$ (1:9)	140
66.7 kppm of system	**half decay time (min)**
surfactant-$scCO_2$	no half time
PECNP:surfactant-$scCO_2$ (4:6)	no half time
PECNP:surfactant-$scCO_2$ (3:7)	no half time
PECNP:surfactant-$scCO_2$ (2:8)	60
PECNP:surfactant-$scCO_2$ (1:9)	30

[a]No half time: No recorded decay to half of the foam height because of stability of the foam system.

and static measurement studies help with understanding of the fluid behavior as fluid flow is mainly affected by flow geometry, time scale, foam microstructure and stability.[55] The rheology of dry CO_2 foam is widely regarded as non-Newtonian.[55,56] To characterize the non-Newtonian nature of $scCO_2$ foam created by the PECNP−surfactant mixture, first, the viscosity is measured at the specific value of shear rate 2000 s^{-1} (Figure 7). The maximum apparent viscosity trend with time was observed for $scCO_2$ foam generated with PECNP:surfactant systems with ratios of 1:9 and 4:6 prepared in 33.3 and 66.7 kppm brines, respectively.

It was previously noted that a high gas volume fraction above the volume fraction of bulk close-packed spheres can significantly increase the viscosity.[57] The bubble deformation at constant shear occurs with a slower rate for the most stable mixtures (1:9 and 4:6), as the surface tension of PECNP at the interface restores the bubble shape.[55] A higher apparent viscosity indicates the formation of smaller bubble sizes and a narrower size distribution,[58] as a result of monodispersed ordered structures formed by the ionic PECNP/surfactant stabilizers in the lamella.[59] Higher shear resistivity originates from the ability of lamella to reverse the deformations as well as energy storage capacity at the interface controlled by chemical components at the CO_2−water interface.[55]

The shear thinning behaviors of PECNP−surfactants were examined with the shear rate sweep test shown in Figure 8. Shear thinning for WLM at high concentrations entangled with flexible polymer chains on the nanoparticle surface was reported to be due to alignment of wormlike chains, which increases the viscoelasticity of the mixture.[25] Wanniarachchi et al. presented the effect of very low and very high viscosity fracture propagation and proppant transport.[60] Although high viscosity foam carries the required amount of proppants to the fracture, it may not be able to penetrate through microfractures with tiny openings, so the moderate viscosity range (50−250 cP) is recommended.[60,61]

Shear thinning properties were evaluated through the laminar flow of incompressible $scCO_2$ foam through a Couette geometry rheometer, and the results were matched by the power law model.[55,62] The apparent viscosity of the foam was reduced with increasing shear rate (shear softening with $n < 1$). Foam lamella drainage is at its lowest for the highest viscosities achieved with PECNP:surfactant solutions with 1:9 ratio in 33.3 kppm and 4:6 in 66.7 kppm, respectively. Xue and co-workers demonstrated the viscous thick lamella's ability in "CO_2- aqueous phase" to lower the rates of Ostwald ripening,[22] which leads to generation of smaller bubbles.[63] The two

DOI: 10.1021/acs.iecr.9b01390
Ind. Eng. Chem. Res. 2019, 58, 9431−9449

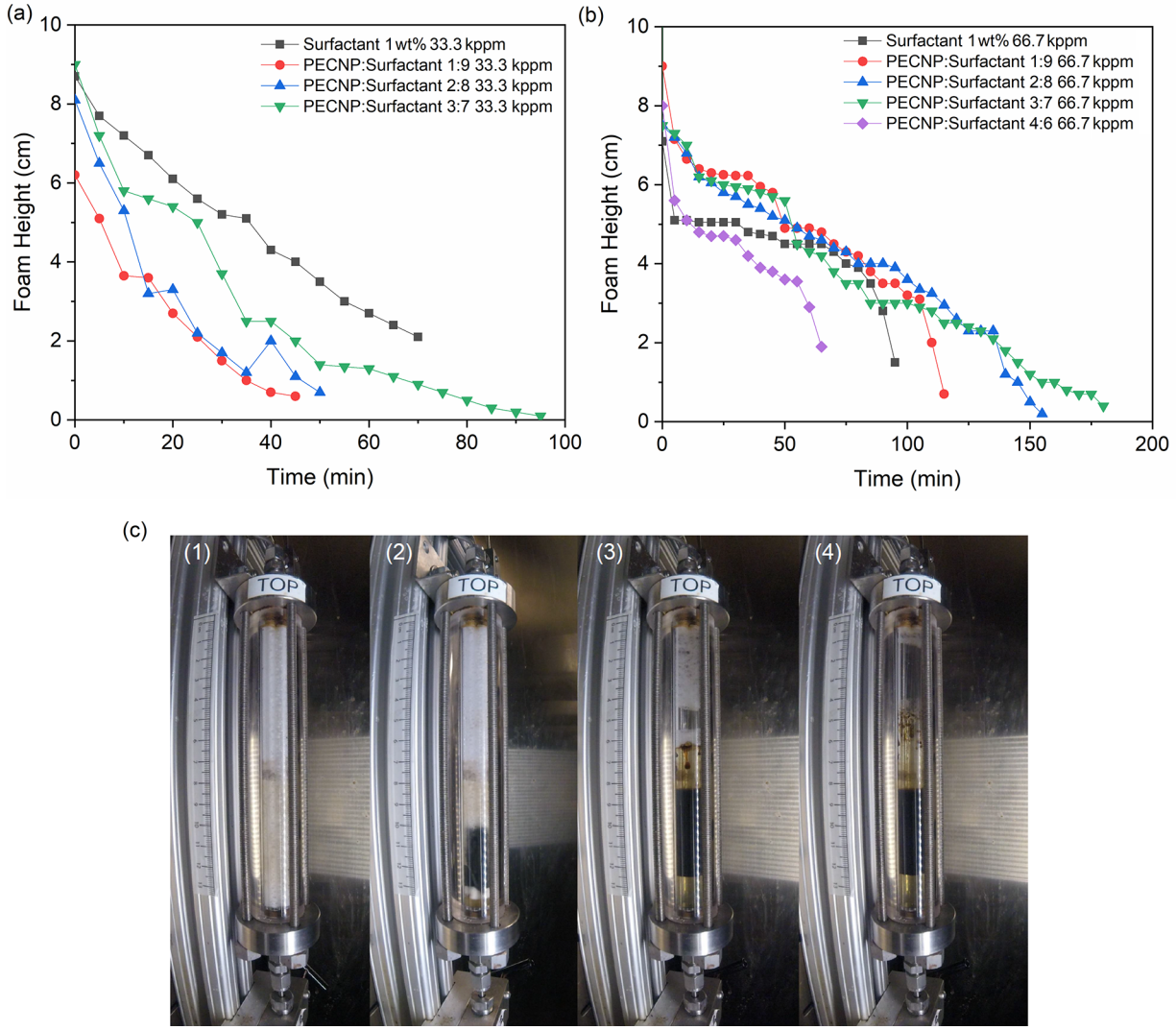

Figure 6. Foam stability measurements in the presence of crude oil for variety of PECNP−surfactant mixtures in (a) 33.3 kppm brine solutions and (b) 66.7 kppm brine solutions. (c-1) Foam generation and isolation in the view cell; (c-2) introduction of the oil; (c-3) foam drainage in the presence of oil; (c-4) total foam disappearance and oil dominance. Reprinted with permission from ref 3. Copyright SPE 2018.

Table 5. Entering and Spreading Coefficients for PECNP and Surfactant Mixtures in the Presence of $scCO_2$ and MLP Crude Oil

33.3 kppm of system	σ_{wg} (mN/m)	σ_{ow} (mN/m)	E (mN/m)	S (mN/m)
brine	33.42	11.47	44.89	21.95
surfactant 1 wt %	6.35	0	6.35	6.35
PECNP	14.97	0.87	15.84	14.1
PECNP:surfactant (1:9)	6.43	0	6.43	6.43
66.7 kppm of system	σ_{wg} (mN/m)	σ_{ow} (mN/m)	E (mN/m)	S (mN/m)
brine	31.45	9.97	41.42	21.48
surfactant 1 wt %	6.55	0	6.55	6.55
PECNP	15.1	1.7	16.8	13.4
PECNP:surfactant (4:6)	6.74	0	6.74	6.74

PECNP−surfactant systems prepared in 33.3 and 66.7 kppm offer higher apparent viscosity and flow consistency indices (Table S4) to enhance proppant transport and placement. Plastic deformation in the bulk fluid shown in Figure 8 is the result of stress-induced bubble slide, coalescence, and coarsening, which are controlled by elastic deformation of the film containing a network of the PECNP−WLMs nanoparticles in the solidlike interface studied by dilatational elasticity measurements (section 3.4). The flow consistency index depicts the highest value for optimal concentrations of PECNP and WLMs (Table S4); therefore, pressure drops across the tubular wellbore, and fractures reach their highest level for optimal values.[64]

The formation of PECNPs as a result of electrostatic complexation of PECNP with WLMs helps to stabilize the water−CO_2 lamella by enhancing the viscosity, rigidity, and electrostatic repulsion among lamellae surfaces.[5] In addition to Ostwald ripening slow down caused by high packing fractions of WLMs,[22] the association of surfactant with nanoparticles enhances the stability and viscosity of foam lamella even further.

3.4. Interfacial Tension Analysis and CMC. Figure 9 reveals the CMC calculations for a variety of surfactant concentrations in 33.3 and 66.7 kppm brine systems according to the analysis of interfacial tension measurements. The determined CMCs are 0.059 wt % for 33.3 kppm brine and

DOI: 10.1021/acs.iecr.9b01390
Ind. Eng. Chem. Res. 2019, 58, 9431−9449

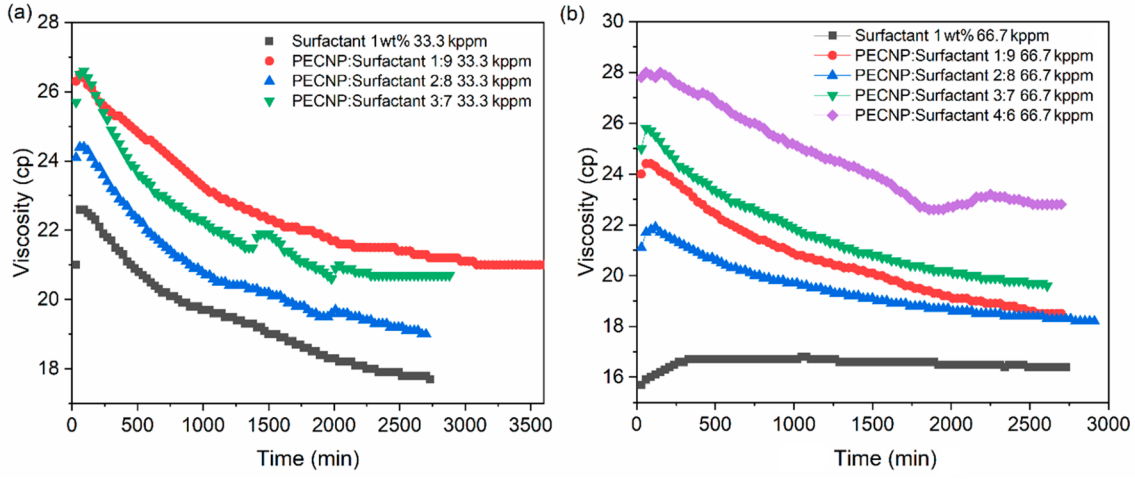

Figure 7. Viscosity with respect to time for 90% $scCO_2$ foam quality generated using 1:9, 2:8, 3:7, and 4:6 ratios of PECNP:surfactant prepared in (a) 33.3 kppm and (b) 66.7 kppm brine (static constant shear measurement). Reprinted with permission from ref 3. Copyright SPE 2018.

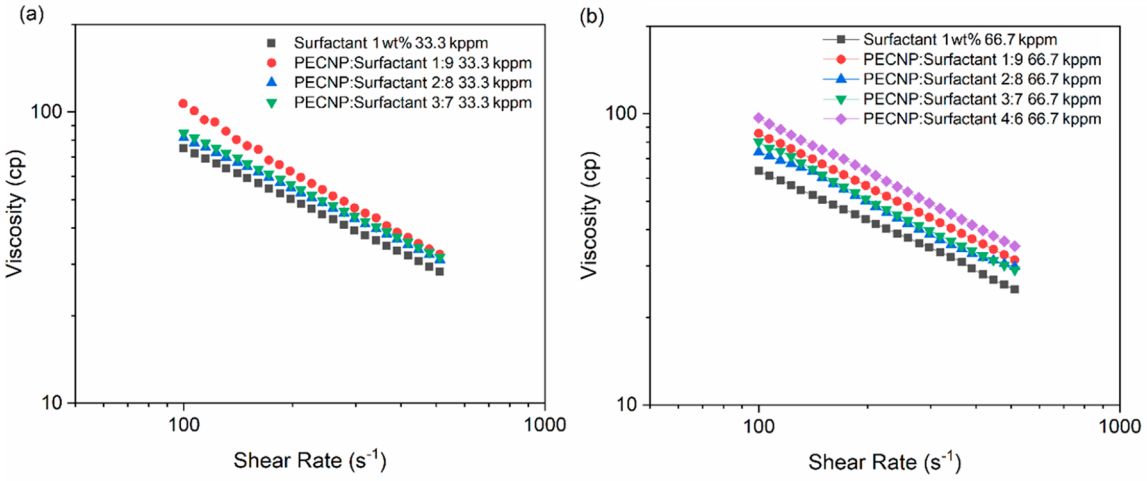

Figure 8. Viscosity with respect to shear rate of 90% $scCO_2$ foam quality systems prepared using 1:9, 2:8, 3:7, and 4:6 ratios of PECNP:surfactant in (a) 33.3 kppm and (b) 66.7 kppm brine (static shear sweep measurement). Reprinted with permission from ref 3. Copyright SPE 2018.

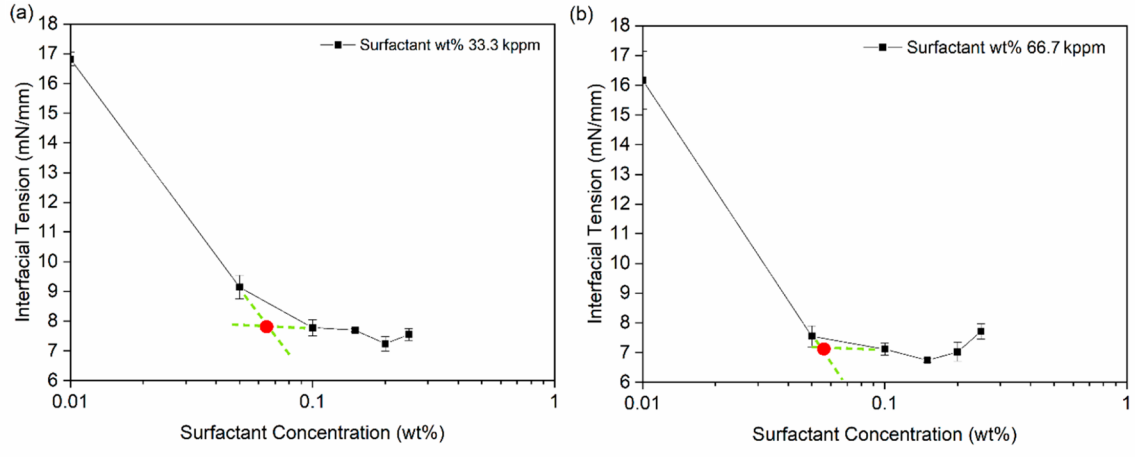

Figure 9. Critical micelle concentration for the viscoelastic surfactant at two different brine salinity values: (a) 33.3 kppm and (b) 66.7 kppm.

0.055 wt % for 66.7 kppm brine. The presence of two charges on the surfactant molecule helps to form the micelles at lower concentrations.[25] Micellar solutions are formed above the CMC in both 33.3 and 66.7 kppm high-salinity brines. The zwitterionic surfactant micelles were found to aggregate into wormlike micelles with self-assembly of surfactant into the elongated structures;[25] thus, WLMs are expected to exist at 1 wt % surfactant in high-salinity brine. It was previously

DOI: 10.1021/acs.iecr.9b01390
Ind. Eng. Chem. Res. 2019, 58, 9431−9449

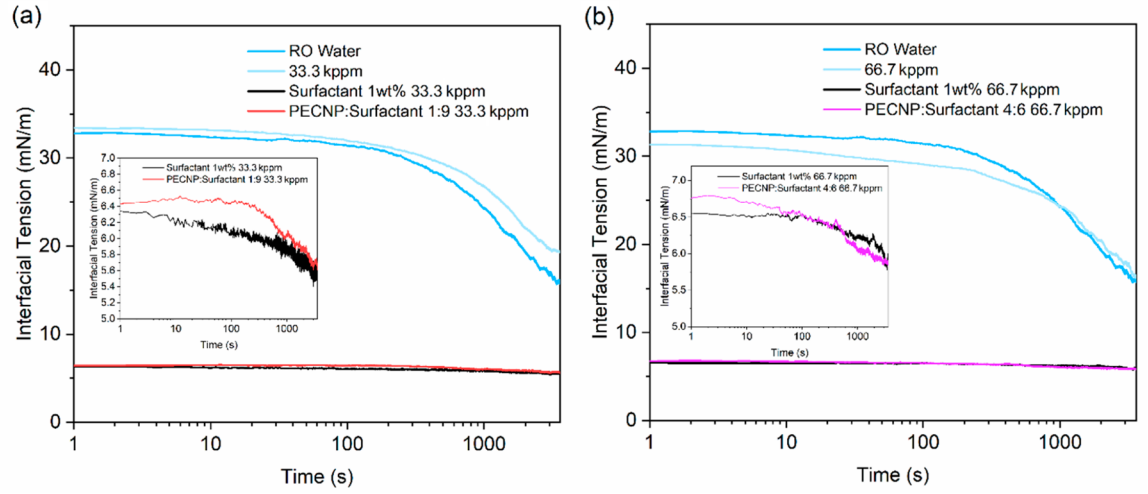

Figure 10. Interfacial tension measured for surfactant and PECNP in (a) 33.3 kppm and (b) 66.7 kppm brine.

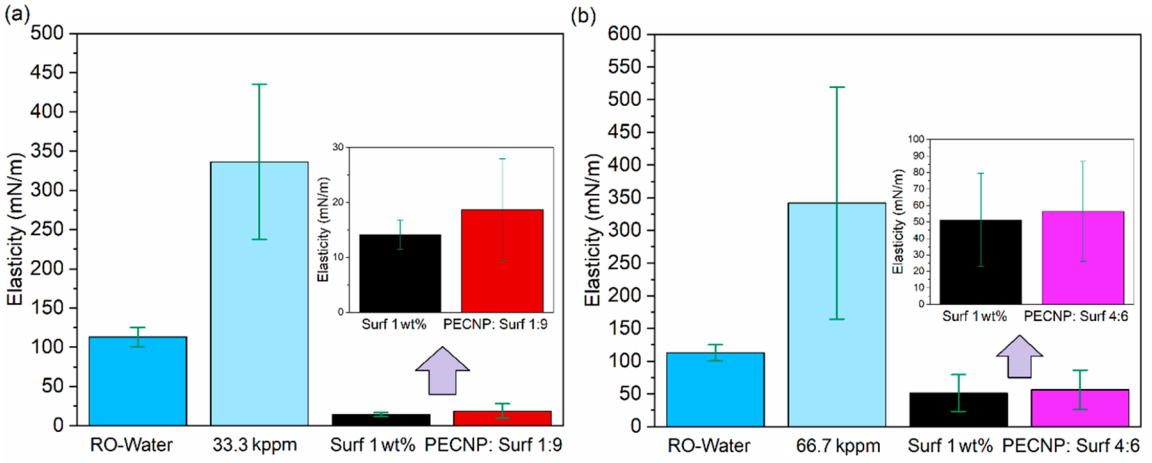

Figure 11. Dilatational elasticity measured for RO water and surfactant and PECNP in (a) 33.3 kppm and (b) 66.7 kppm brine according to interfacial tension analysis.

reported that salt ions would screen the electric double layer around the micelles and negatively affect the micellar assembly;[40] however, the ionic activity of zwitterionic surfactant gives rise to the effective micellar volume fraction. Therefore, CMC is still achieved at low concentrations.

Interfacial tension analysis results for $scCO_2$ bubbles formed in 1 wt % surfactant and PECNP in 33.3 and 66.7 kppm brine systems suggest that the interfacial tension dramatically declines upon addition of surfactant and PECNP:surfactant (Figure 10a,b). The very low IFT values of 5.4 and 6.4 mN/mm were obtained after addition of 1 wt % surfactant and PECNP:surfactant, with 1:9 ratio, to 33.3 kppm brine because of interfacial stabilization of $scCO_2$−brine lamella by improving repulsive forces created using ionic micelles, wormlike micellar self-assembly with PECNP, and the network layer formed in the lamella. The IFT decline hits the minimum value (5.5 mN/mm) in lower concentration of ionic salts (33.3 kppm), whereas at higher concentrations (66.7 kppm), because of higher presence of ionic interactions and imbalanced forces, a slightly higher IFT value was detected. Addition of WLMs further stabilizes the $scCO_2$ lamella because of micellar branching and intra-aggregate attractions which lower the perturbations and imbalanced forces at the interface, as reported by Boury and Tewes.[39,65] Polymeric nanoparticles present in the lamella in conjunction with WLMs form vesicular nanocapsules in which ionic aggregates reorient from the bulk phase to the lamella border and form arrays of stabilized PECNPs lining up on the interface between the supercritical phase and aqueous phase. While PECNPs do not necessarily reduce the IFT at the interface, one should note PECNP−surfactant nanoparticles are not a driving force for lamella instability and imbalanced forces at the interface; therefore, the ionic compatibility and stability are preserved.

The dilatational elasticity was measured for RO water, surfactant, and PECNP in (a) 33.3 kppm and (b) 66.7 kppm brine according to eq 1) using dynamic interfacial tension measurements with $scCO_2$ (Figure 11). Dilatational elasticity represents the surface tension gradient which opposes the film drainage and provides a more stable film along the CO_2−water interface.[40] High values of surface elasticity do not guarantee the counterbalance of surfactant adsorption and surface diffusion to surface tension gradient and velocity of film thinning;[40] thus, the surface tension variation at the interface with respect to area change needs to fall within the allowable range to oppose the destabilizing forces.[65,66]

Similar to IFT, the equilibrium surface dilatational elasticity is significantly lower than RO water and high-salinity brines, when WLMs and PECNP−WLM mixtures exist in the CO_2−

DOI: 10.1021/acs.iecr.9b01390
Ind. Eng. Chem. Res. 2019, 58, 9431−9449

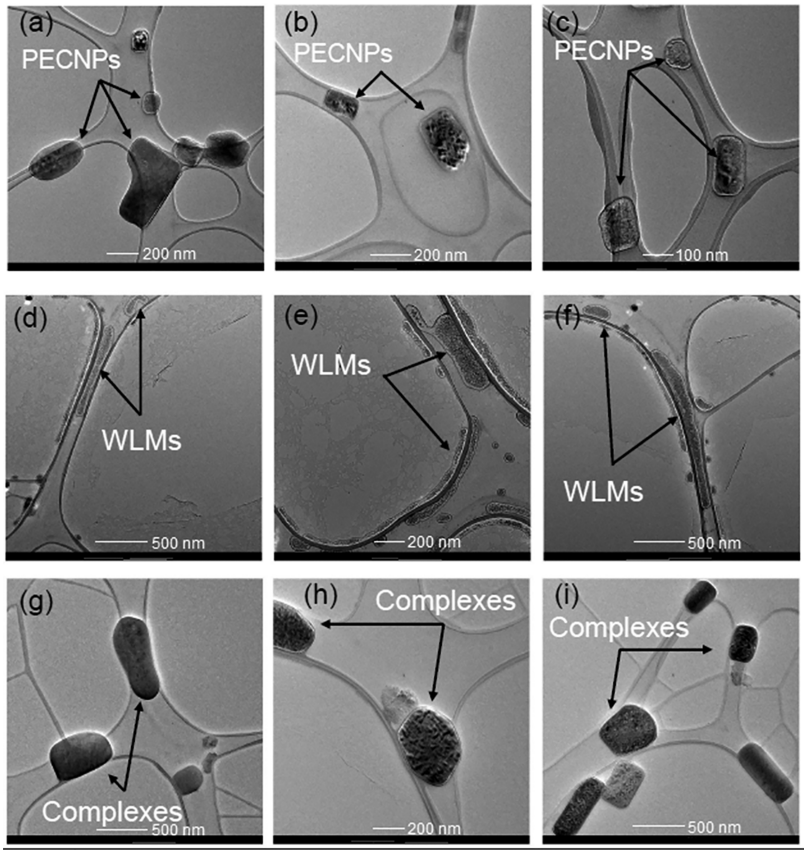

Figure 12. TEM images for PECNP nanoparticle (a–c), 1 wt % surfactant (d–f), and complexes of PECNP:surfactant 1:9 (g–i) prepared in 33.3 kppm high-salinity brine. The semidried mixtures were examined on a copper grid.

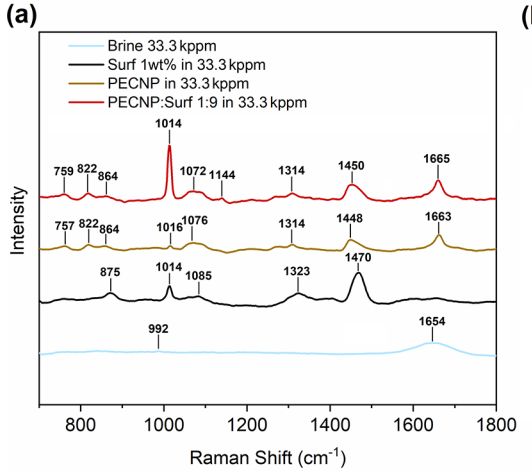

(b)

Raman shift (cm^{-1})	Vibrational mode/Assignment
992 (free, aqueous) 1014 (bound)	$\nu_1 SO_4$
600-1300	νC-C (aliphatic chain vibrations)
1200-1340	δN-H (Amide III) νC-N stretch
1400-1470	δCH_2, δCH_3 asym
1510-1580	νC-N, δN-H (Amide II)
1640	δH_2O
1680-1820	δN-H (Amide I) νC=O

Figure 13. Identified bands and corresponding assignments in Raman spectra for 33.3 kppm brine, surfactant, PECNP, and PECNP:surfactant (1:9) in brine (a) and identification of key Raman band (b) corresponding groups based on the values reported in the literature.[68,69]

water interface (Figure 11). The difference between the elasticity obtained by WLMs and PECNP–WLM is not considerable, though addition of PECNP slightly increases the value as an indication of infinitesimal rigidity added to the interface, when PECNP–WLMs agglomerates form networks at the interface, giving rise to lamella elasticity and prolonging the bubble rupture time.

3.5. Transmission Electron Microscopy. Morphological representations of nanoparticles and surfactants in high-salinity brines agree with the light-scattering and Raman spectroscopy observations presented in sections 3.1 and 3.6. Figure 12 shows the TEM images for PECNP, 1 wt % surfactants, and PECNP–surfactant (with 1:9 ratio) prepared in 33.3 kppm high-salinity brine. Formation of PECNPs as particles made by electrostatical interaction between PEI and DS is visible in Figure 12a–c. The size range of PECNPs is consistent with the predicted values of dynamic light-scattering measurements (section 3.1). The 1 wt % surfactant solution in the high-salinity brine exhibits the formation of WLMs as elongated rodlike surfactant aggregates (Figure 12d–f).

DOI: 10.1021/acs.iecr.9b01390
Ind. Eng. Chem. Res. 2019, 58, 9431–9449

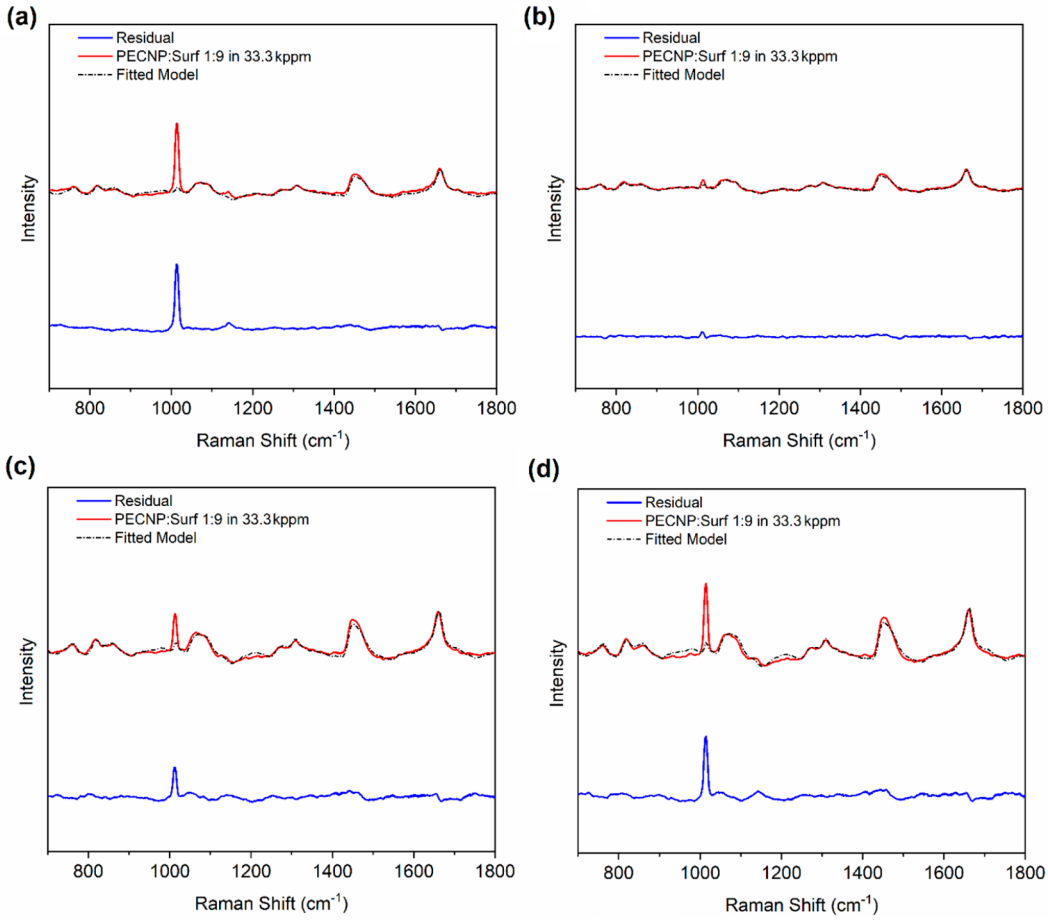

Figure 14. Raman spectra of four PECNP:surfactant 1:9 samples (red) fit with average PECNP and surfactant spectra (black dots) and corresponding residual (blue).

Initially, nanoparticle agglomerates with WLMs form ringlike structures. WLMs are formed and coiled in the presence of nanoparticles starting to merge with the nanoparticle as they cover the outermost layer of a PECNP. Decoration of micelles on nanoparticles is derived through the redistribution and direct adsorption of micelles on nanoparticles due to electrostatic attractions between the amine and sulfonate groups, confirmed by Raman spectroscopy (section 3.6). With time, the PECNP helps to form an elastic layer at the interface to overcome the foam coarsening as accumulation of elastic and positively charged hydrophilic particles at the plateau border hinders liquid drainage. Formation of stable nanogels in the form of vesicular structures (sphere-to-rod transition) was previously shown and studied in molecular dynamic simulations in cetyltrimethylammonium chloride (CTAC)-functionalized NP self-assembly,[25,67] where double-layer coverage of WLMs on oppositely charged and spherical nanoparticles induces the self-assembly of nanoparticle−surfactant in an aqueous medium.

3.6. Raman Spectroscopy. Figure 13 illustrates the identified characteristic bands in Raman spectra and corresponding functional groups for the mixtures of PECNP and 1 wt % surfactant prepared in 33.3 kppm brine.

The PECNP and surfactant spectra share many of the same bands, corresponding to their backbones and other shared functional groups. Of special note are the 1014 and 1665 cm^{-1} bands. The first represents a totally symmetric sulfate stretching mode associated with the surfactant (present to a very minor extent in the PECNP spectrum because of the dextran sulfate used to make the PECNP), while the second band represents the δN−H in-plane bending generated by the nitrogen−hydrogen bonds and is unique to the polyehtyleneimine. A band around 1654 cm^{-1} is observed in the brine (and underlying some of the other spectra) that can be attributed to the remaining water present in the lyophilized samples.[70,71] The 33.3 kppm brine spectrum has a weak band for free sulfate (SO_4^{-2}) from Na_2SO_4 centered at 992 cm^{-1}.[72] The chemically bound sulfate band can be found at 1014 cm^{-1} in the three other spectra as that functional group is found in both the surfactant and the dextran sulfate used to make the PECNPs, although the relative intensity of this band varies significantly among the spectra. This observed shift is consistent with previously reported findings by Wang and co-workers[73] about the noticeable band shift for the SO_4^{2-} band from 992 to 1010 cm^{-1} in titanium hydroxide complexation with sulfate.

In order to better understand the changes in intensity of the sulfate signal, especially in the PECNP−surfactant spectrum, a simple model was developed. Using least-squares fitting, four PECNP:surfactant 1:9 Raman spectra (collected from different locations within the lyophilized samples) were fit with average PECNP and surfactant spectra. The residual of corresponding fit indicates locations within the spectra where the PECNP:surfactant spectrum is not completely explained by the sum of the components. If the PECNP:surfactant spectrum represented a mixture, rather than a change in chemistry, then its residual should represent the noise in the data;

DOI: 10.1021/acs.iecr.9b01390
Ind. Eng. Chem. Res. 2019, 58, 9431−9449

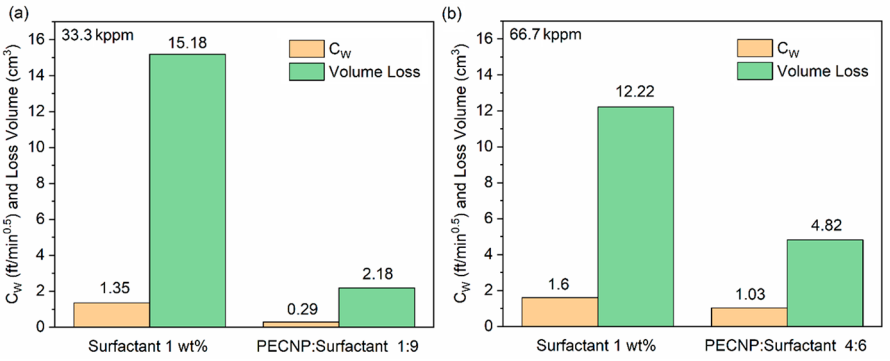

Figure 15. Total fluid loss (gas and liquid) and fluid loss coefficient for the mixtures prepared in (a) 33.3 kppm and (b) 66.7 kppm high-salinity brines.

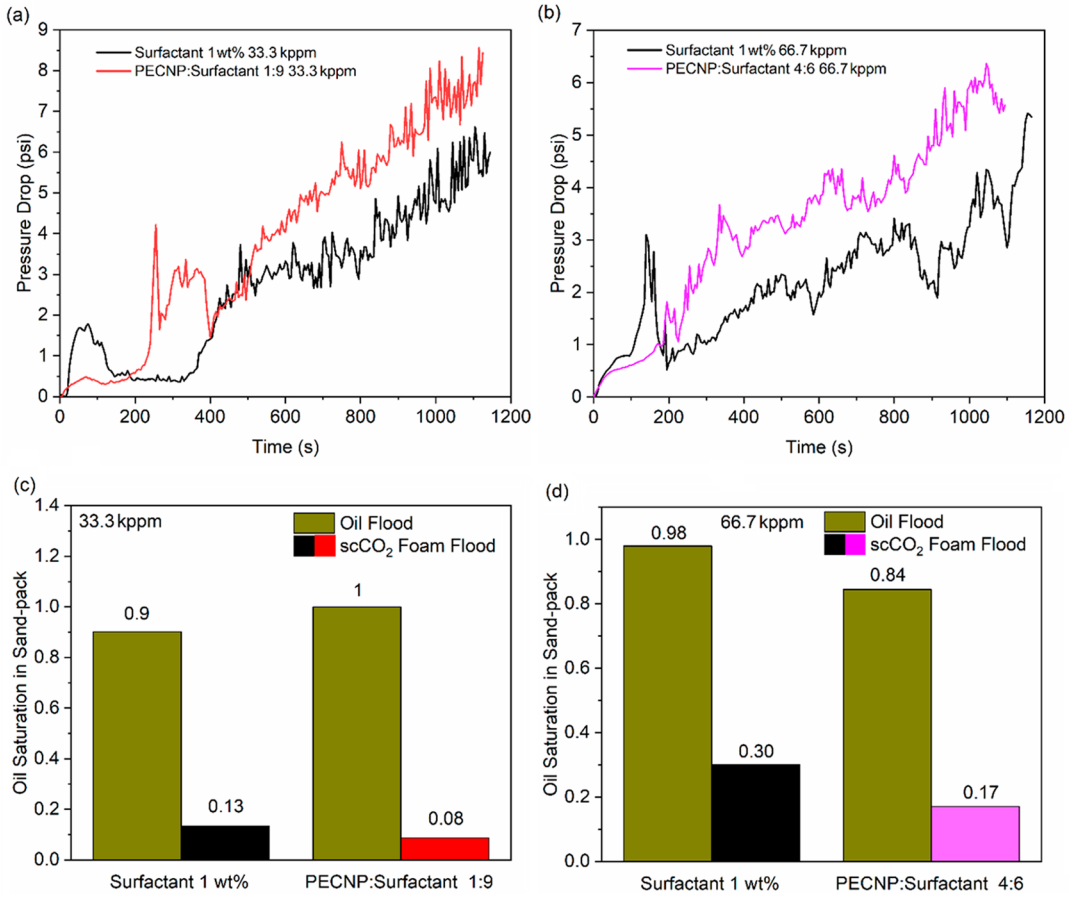

Figure 16. Foam pressure drop and saturation profile for $scCO_2$ foams generated by surfactant and PECNP−surfactants in high-salinity brine. (a) Pressure drop profile for foam flood inside the oil saturated sand pack in 33.3 kppm brine (b) Pressure drop profile for foam flood inside the oil saturated sand pack in 66.7 kppm brine (c) Oil saturation in sand pack after oil flood and foam flood for cleanup in 33.3 kppm brine (d) Oil saturation in sand pack after oil flood and foam flood for cleanup.

however, this is clearly not the case, as shown in Figure 14. In each residual, the sulfate band at 1014 cm^{-1} stands out as significantly different, indicating that complexation between the PECNP and the surfactant occurs and that the complex itself has a unique Raman signature (possibly because of a change in chemical environment of the key functional groups). The strength of the sulfate band varies between samples; however, as the complexes are not homogeneous, this should not be a surprise. There are other minor changes to peaks within the Raman spectrum, particularly at 1144 cm^{-1}, indicating that the changes due to complexation are not confined to the polyatomic anions.

Taken together, the IR spectra (Figure S2) and Raman data indicate the surfactant structure resembles the amidopropyl hydroxysultaine with a long hydrophobic tail, sulfonate, and quaternary ammonium pendant groups. The main functional groups are quaternary and secondary amines as well as pendant hydroxide groups, amide, and sulfonate ($R\text{-}SO_3^-$). The combination of ammonium and sulfonate offers a zwitterionic surfactant with both cationic and anionic charge head groups

DOI: 10.1021/acs.iecr.9b01390
Ind. Eng. Chem. Res. 2019, 58, 9431−9449

capable of conjunction with PECNP in $scCO_2$ lamella interface.

3.7. Dynamic Fluid Loss. It is critical to control the leak-off rate of fracturing fluids to reduce pumping cost and to ensure the mechanical integrity of the formation. Production from horizontal wells in tight reservoirs requires high internal fracture conductivity because conductivity provides a path to accommodate high-velocity hydrocarbon flow.[74] Fluid loss coefficients were measured with the setup presented in Figure 3 for the $scCO_2$ foams prepared with highest apparent and dynamic viscosities (1:9 ratio and 4:6 ratio of PECNP:surfactant in 33.3 and 66.7 kppm brine systems, respectively), and the results are shown in Figure 15.

The initial and final permeabilities of a Kentucky sandstone tight core exposed to the flow of $scCO_2$ foam with PECNP−surfactant remained constant (0.18 mD), revealing minimal pore throat plugging and damage to the core as a result of core exposure to the fracturing fluid. The fluid loss volume and fluid loss coefficients were significantly lowered when PECNP−surfactant was used as the aqueous component of the foaming solution as compared to surfactant alone, resulting in a reduced leaked volume in the tight core and enhanced fracture properties. The fluid loss coefficient is a function of core permeability, surfactant/PECNP concentration, and temperature.[75] Furthermore, it was previously reported that higher foam quality provides higher viscosity and reduced leak-off.[76] Efficient merge of WLMs to PECNPs resulted in the formation of nanoparticles performing as fluid loss additives during the injection of the foam solutions. The results were consistent with rheological measurements where PECNP−surfactant systems prepared in 33.3 and 66.7 kppm brine exhibited the highest viscosities over the shear thinning period. It was previously argued that osmotic pressure, which leads to the foam's tendency to retain water, prevents the water leak-off to the formation;[77] thus, it can be concluded that PECNP−WLMs enhance the proppant carrying capability of $scCO_2$ foam while lowering the water usage.

3.8. Sand Pack Measurements. The detailed flooding scenarios and mobility features in the sand pack experiment are indicated in Table S6. The permeability of the pack after an initial brine flood with 33.3 and 66.7 kppm brine varies between 144 and 170 D; on the basis of Darcy's law, the value represents a high-permeability porous pack (Supporting Information). The apparent viscosity of fracturing fluid in the pack is calculated according to Darcy's equation (eq 6):

$$\mu_{app} = \frac{kA\Delta P}{QL} \tag{6}$$

where k is permeability of the fluid inside the pack, ΔP the pressure difference between the two ends of the pack, A the cross-sectional area of the pack, Q the volumetric flow rate of fracturing fluid flow in the pack column, and L the pack length. Accordingly, the apparent viscosity is obtained, and the results are shown in Table S6. Upon oil saturation, 10 pore volumes of crude oil was flooded to completely saturate the pack. The efficiency of the oil flood varied between 84 and 100%. Consequently, the $scCO_2$ foam was flooded to clean up the oil-saturated pack. Foam breakthrough occurred at 5.9 and 5.35 PV of foam flood for 33.3 and 66.7 kppm brines, respectively, representing a better oil cleanup and sweep efficiency for 33.3 kppm salinity $scCO_2$ foams as a result of the foam half decay time and higher viscosity shown in Tables 4 and S4.

The pressure drop is recorded during the propagation of oil or $scCO_2$ foam through the sand pack. Figure 16a,b exhibits the magnitude of the pressure drop with respect to time of foam flood. Relative stability, propagation, and performance of the $scCO_2$ foam in the pack helped to effectively mobilize and recover the crude oil in the fractured reservoirs. Accordingly, large effective viscosities and sufficient mobility control for PECNP−surfactant enhanced $scCO_2$ foam are concluded.

The saturation of oil and water phase in the pack after the oil flood is calculated from the following sets of equations:

$$S_{o1} = \frac{V_{oi} - V_{oc} - V_{P2} - V_{P1}}{PV} \tag{7}$$

and

$$S_{w1} = 1 - S_{o1} \tag{8}$$

where S_{o1} is the oil saturation in the pack, V_{oi} the injected volume of oil through the lines and pack, and V_{oc} the collected volume of oil in the outlet after the oil flood. V_{P1} and V_{P2} are spurt volumes of inlet and outlet lines connected to the pack. S_{w1} is the remaining saturation of aqueous phase in the pack. PV is pore volume of ceramic proppants in the pack. Likewise, the saturation of oil and water phase in the pack after the foam flood is shown as

$$S_{o2} = S_{o1} - \frac{V_{ocf} - V_{P2} - V_{P1}}{PV} \tag{9}$$

and

$$S_{w2} = 1 - S_{o2} \tag{10}$$

where S_{o2} and V_{ocf} are the oil saturation and collected oil volume.

The oil saturation is measured before and after foam flood with 1 wt % surfactant, and PECNP−surfactant enhanced $scCO_2$ foam is shown in Figure 16c,d. The initial oil saturation varies between 0.84 and 1 depending on the available pore volume and packing efficiency. The secondary oil saturation drops to lower values after the surfactant foam flood is performed, indicating the capability of the foam to clean up the pack. Efficiency of the cleanup improves with 1:9 and 4:6 PECNP−surfactant $scCO_2$ foam as oil saturation drops by 85 to 92% in 33.3 kppm systems (Figure 16c) and by 69 to 86% in 66.7 kppm systems (Figure 16d). The results are consistent with the apparent and shear viscosities presented in Figures 7 and 8 where 1:9 and 4:6 ratios exhibit the capacity for cleanup and oil improvement of sweep efficiency. It is concluded that enhanced viscosity as a result of bulk foam stability using PECNP−surfactant improves the dynamics of foam flow in porous media.

4. CONCLUSIONS

Herein, we reported the results of a responsive $scCO_2$ foam which combines improved viscosity and stability to carry proppants as well as instability in the presence of the oil phase, resulting in rapid degradation upon contact. A novel mixture containing PECNP−surfactant in high-salinity brine was successfully prepared to enhance $scCO_2$ foam, reduce formation damage, and improve cleanup properties during the hydraulic fracturing process. The major conclusions can be summarized as follows:

(1) The presented mixture overcomes the traditional issues of water-based foam liquids such as foam instability at high

DOI: 10.1021/acs.iecr.9b01390
Ind. Eng. Chem. Res. 2019, 58, 9431−9449

temperature and pressure and formation damage due to high water content. It offers a perfect compatibility of $scCO_2$ with high-salinity produced waters (divalent ions) up to 67 kppm TDS (higher than sea level) to minimize the amount of fresh water use and produced water disposal in the hydraulic fracturing process, helping to create a sustainable process of oil recovery from tight shale formations and to store large volumes of CO_2 from the atmosphere.

(2) Minimum polyelectrolyte and surfactant concentrations are required for effective performance with the recommended PECNP−surfactant mixture. A zwitterionic surfactant resistant to high temperatures, compatible with high-salinity brine and charged nanoparticles, was employed to interact with PECNPs electrostatically. The mixture lowers the surface tension of $scCO_2$ bubbles up to 74% in 33.3 kppm and 93% in 66.7 kppm high-salinity brines.

(3) The formation of vesicular complexes as a result of electrostatic complexation of PECNP with WLMs was visually identified with TEM images and confirmed with Raman spectroscopic results. The ionic complexes are capable of stabilizing the water−CO_2 lamella by enhancing the viscosity (rheometry), rigidity (dilatational elasticity), and electrostatic repulsion (zeta potential measurements) among lamellae surfaces. A least-squares fitting algorithm as morphological model proved the synergistic complexation between PECNP and surfactant based on fitting analysis on acquired Raman spectra from ionic mixtures. The underlying mechanism was identified as electrostatic rearrangement of WLMs along the structure of PECNP to form electrostatically bonded layers with nanoparticles and create a stable complex.

(4) The stability of $scCO_2$ bubbles is improved through the formation of electrostatically enhanced bubbles containing the aggregates of PECNP−surfactant. The foam stability drastically improved in the view cell test as optimum mixtures presented longer foam lifetime. PECNP−surfactant mixtures represent a new prospect for stabilizing the bubble film in a high-salinity environment and the tailoring of the lamella repulsive forces through addition of different PECNP-to-surfactant ratios to overcome the lamella drainage and film thinning.

(5) Fluid loss commonly occurring in the fracturing process can be controlled using the presented PECNP−surfactant $scCO_2$ foam. Fluid loss volume and fluid loss coefficients for CO_2 and water were lowered up to 86 and 78%, respectively, by employing PECNP−surfactant resulting in lower formation damage.

(6) Rapid and easy cleanup is offered by PECNP−surfactant $scCO_2$ foam when the high pressure drop and decline in oil saturation were detected in sand pack tests.

■ ASSOCIATED CONTENT

Supporting Information

The Supporting Information is available free of charge on the ACS Publications website at DOI: 10.1021/acs.iecr.9b01390.

Brief explanation of experimental procedures, functional characterization of surfactant, process flow diagram for air foam stability setup and results, supplementary physical property measurement for PECNP and PECNP/surfactant mixtures, additional dilatational elasticity and sand pack calculations, and supplementary data for Raman spectroscopy (PDF)

■ AUTHOR INFORMATION

Corresponding Author

*E-mail: rezab@ku.edu. Phone: (785)864-1232.

ORCID

Hooman Hosseini: 0000-0002-5072-6737

Reza Barati Ghahfarokhi: 0000-0002-1064-9562

Notes

The authors declare no competing financial interest.

■ ACKNOWLEDGMENTS

The authors are grateful to the National Science Foundation (no. 123350) for providing financial support. The project is funded by National Science Foundation EPSCor Research Infrastructure Improvement Program: Track-2 Focused EPSCoR Collaboration Award (OIA- 1632892). Authors acknowledge Harcros Chemicals for providing the surfactant used in this work. Authors also extend their appreciation to Dr. Cory J. Berkland, Matthew Christopher, and Stephanie Johnson in the Pharmaceutical Chemistry Department at University of Kansas (KU) for their generous help in freeze-drying of samples, Dr. Qiang (Charles) Ye for his support with FTIR and Raman spectroscopic measurements performed at Institute for Bioengineering Research (IBER) Laboratories at University of Kansas, and Carson Rufledt for Raman spectroscopy analysis in the KU Department of Geology. The endeavors of Zach Kessler, Jeff Worth, and Scott Ramskill from Chemical and Petroleum Engineering Department and Tertiary Oil Recovery Program (TORP) at the University of Kansas are appreciated. Last but not the least, the authors gratefully acknowledge Dr. Prem S. Thapa from KU Microscopy and Analytical Imaging Laboratory for help with transmission electron microscopy analysis.

■ ABBREVIATIONS

$scCO_2$ = supercritical CO_2
CCUS = carbon capture utilization and storage
VES = viscoelastic surfactant
WLM = wormlike micelle
PEI = polyethylenimine
DS = dextran sulfate
PECNP = polyelectrolyte complex nanoparticle
MLP = Mississippian limestone play
RO−DI water = reverse osmosis and deionized water
CMC = critical micelle concentration
FTIR = Fourier transform infrared spectroscopy
MMP = minimum miscibility pressure
TEM = transmission electron microscopy
IFT = interfacial tension
TDS = total dissolved solids

■ NOMENCLATURE

ϕ = gas volume fraction
$\Delta\pi_e$ = equilibrium part of surface pressure variation (mN/m)
$\Delta\pi_{ne}$ = nonequilibrium part of surface pressure variation (mN/m)
E_e = equilibrium surface dilatational elasticity (mN/m)
U_b = velocity of compression (m/s)
A_i = initial surface area (m^2)
t = time (s, min)
τ = relaxation time (s)
V_L = fluid loss volume (cm^3)

DOI: 10.1021/acs.iecr.9b01390
Ind. Eng. Chem. Res. 2019, 58, 9431−9449

C_W = fluid loss coefficient (ft/min$^{1/2}$)
S_p = spurt volume (cm^3)
σ_{wg} = water−gas surface tension (mN/m)
σ_{ow} = oil−water surface tension (mN/m)
σ_{og} = oil−gas surface tension (mN/m)
E = entering coefficient (mN/m)
S = spreading (mN/m)
μ_{app} = apparent viscosity of fluids (cP)
ΔP = pressure difference between the two ends of the pack (psi)
A = cross section area of the pack (cm^2)
Q = volumetric flow rate of fracturing fluid flow (cm^3/s)
L = pack length (cm)
PV = pore volume (cm^3)
k = permeability (D)
S_o = saturation of oil in the pack
S_w = saturation of water in the pack
V_O = volume of oil in the pack (cm^3)
V_{p1} = volume of inlet lines to the pack (cm^3)
V_{p2} = volume of lines in outlet of the pack (cm^3)
V_{oc} = collected volume of oil in the outlet after oil flood (cm^3)
V_{ocf} = collected volume of oil in the outlet after foam flood (cm^3)
K = flow consistency index (Pa·S^n)
n = flow behavior index
η = viscosity (cP)
$\dot{\gamma}$ = shear rate (s^{-1})

REFERENCES

(1) Scanlon, B. R.; Reedy, R. C.; Nicot, J. P. Comparison of water use for hydraulic fracturing for unconventional oil and gas versus conventional oil. *Environ. Sci. Technol.* **2014**, *48* (20), 12386−12393.
(2) *Hydraulic Fracturing*; Smith, M. B.; Montgomety, C. T.; CRC Press, Taylor & Francis Group: New York, 2015.
(3) Hosseini, H.; Tsau, J.; Barati, R. Lowering Fresh Water Usage in Hydraulic Fracturing by Stabilizing scCO$_2$ Foam with Polyelectrolyte Complex Nanoparticles Prepared in High Salinity Produced Water. *Society of Petroleum Engineers.* **2018**, SPE-189555-MS.
(4) Yekeen, N.; Padmanabhan, E.; Idris, A. K. A review of recent advances in foam-based fracturing fluid application in unconventional reservoirs. *J. Ind. Eng. Chem.* **2018**, *66*, 45−71.
(5) Al-Muntasheri, G. A.; Feng, L.; Hull, K. L. Nanoparticle-Enhanced Hydraulic-Fracturing Fluids: A Review. *SPE Prod Oper.* **2017**, *32*, 186−195.
(6) *Hydraulic Fracturing for Oil and Gas: Impacts from the Hydraulic Fracturing Water Cycle on Drinking Water Resources in the United States*; US Environmental Protection Agency - US EPA: Washington, DC, 2016.
(7) Clifford, P. J.; Mellor, D. W.; Jones, T. J. Water Quality Requirements for Fractured Injection Wells. *Society of Petroleum Engineers.* **1991**, SPE-21439-MS.
(8) Gross, S. A.; Avens, H. J.; Banducci, A. M.; Tvermoes, B. E.; Panko, J. M. Surface Spills in Hydraulic Fracturing Operations and Recommendations for Safety Management. *Society of Petroleum Engineers.* **2013**, ASSE-13-558.
(9) Carter, K.; Hammack, R.; Hakala, J. Hydraulic Fracturing and Organic Compounds-Uses, Disposal and Challenges. *Society of Petroleum Engineers.* **2013**, SPE-165692-MS.
(10) Gupta, D. V. S. Unconventional Fracturing Fluids for Tight Gas Reservoirs. *Society of Petroleum Engineers.* **2009**, SPE-119424-MS.
(11) Gupta, D. V. S.; Carman, P. S.; Hughes, B. Associative Polymer System Extends the Temperature Range of Surfactant Gel Frac Fluids. *Society of Petroleum Engineers.* **2011**, SPE-141260-MS.
(12) Alajmi, M. D.; Mahsoon, A. H.; Al-Hajri, N. M. Feasibility Study of Utilizing Hydraulic Turbines to Recover Excess Power. *Society of Petroleum Engineers.* **2016**, SPE-182798-MS.
(13) Ribeiro, L.; Sharma, M. M. A New Three-Dimensional, Compositional, Model for Hydraulic Fracturing with Energized Fluids. *Society of Petroleum Engineers.* **2012**, SPE-159812-MS.
(14) Qajar, A.; Xue, Z.; Worthen, A. J.; Johnston, K. P.; Huh, C.; Bryant, S. L.; Prodanović, M. Modeling fracture propagation and cleanup for dry nanoparticle-stabilized-foam fracturing fluids. *J. Pet. Sci. Eng.* **2016**, *146*, 210−221.
(15) Rezaei, F.; Lawson, S.; Hosseini, H.; Thakkar, H.; Hajari, A.; Monjezi, S.; Rownaghi, A. A. MOF-74 and UTSA-16 film growth on monolithic structures and their CO$_2$ adsorption performance. *Chem. Eng. J.* **2017**, *313*, 1346−1353.
(16) Kang, D.; Lee, M. G.; Jo, H.; Yoo, Y.; Lee, S. Y.; Park, J. Carbon capture and utilization using industrial wastewater under ambient conditions. *Chem. Eng. J.* **2017**, *308*, 1073−1080.
(17) Barati, R.; Liang, J. T. A review of fracturing fluid systems used for hydraulic fracturing of oil and gas wells. *J. Appl. Polym. Sci.* **2014**, *131* (16), 1−11.
(18) Gandossi, L. *An overview of hydraulic fracturing and other formation stimulation technologies for shale gas production*; Publications Office of the European Union: Luxembourg, 2013.
(19) Rochelle, C. A., Moore, Y. A. *The solubility of supercritical CO$_2$ into pure water and synthetic Utsira porewater*; British Geological Survey: Keyworth, Nottingham, 2002.
(20) Nguyen, V. H.; Kang, C.; Roh, C.; Shim, J. J. Supercritical CO$_2$-Mediated Synthesis of CNT@Co$_3$O$_4$ Nanocomposite and Its Application for Energy Storage. *Ind. Eng. Chem. Res.* **2016**, *55* (27), 7338−7343.
(21) Barbati, A. C.; Desroches, J.; Robisson, A.; McKinley, G. H. Complex Fluids and Hydraulic Fracturing. *Annu. Rev. Chem. Biomol. Eng.* **2016**, *7*, 415−453.
(22) Xue, Z.; Worthen, A. J.; Da, C.; Qajar, A.; Ketchum, I. R.; Alzobaidi, S.; Huh, C.; Prodanovic, M.; Johnston, K. P. Ultradry Carbon Dioxide-in-Water Foams with Viscoelastic Aqueous Phases. *Langmuir* **2016**, *32*, 28−37.
(23) Breward, C. J. W.; Howell, P. D. The drainage of a foam lamella. *J. Fluid Mech.* **2002**, *458*, 379−406.
(24) Osei-Bonsu, K.; Shokri, N.; Grassia, P. Foam stability in the presence and absence of hydrocarbons: From bubble- to bulk-scale. *Colloids Surf., A* **2015**, *481*, 514−526.
(25) Dreiss, C. A.; Feng, Y.*Wormlike Micelles*; The Royal Society of Chemistry; Cambridge, U.K., 2017.
(26) William, J. K. M.; Ponmani, S.; Samuel, R.; Nagarajan, R.; Sangwai, J. S. Effect of CuO and ZnO nanofluids in xanthan gum on thermal, electrical and high pressure rheology of water-based drilling fluids. *J. Pet. Sci. Eng.* **2014**, *117*, 15−27.
(27) Vryzas, Z.; Mahmoud, O.; Nasr-El-Din, H. A.; Kelessidis, V. C. Development and Testing of Novel Drilling Fluids Using Fe$_2$O$_2$ and SiO$_2$ Nanoparticles for Enhanced Drilling Operations. *Society of Petroleum Engineers.* **2015**, IPTC-18381-MS.
(28) Cai, J.; Chenevert, M. E.; Sharma, M. M.; Friedheim, J. E. Decreasing Water Invasion Into Atoka Shale Using Nonmodified Silica Nanoparticles. *SPE Drill Complet.* **2012**, *27* (1), 103−112.
(29) Haroun, M. R.; Alhassan, S.; Ansari, A. A.; Al Kindy, N. A. M.; Abou Sayed, N.; Abdul Kareem, B. A.; Sarma, H. K. Smart Nano-EOR Process for Abu Dhabi Carbonate Reservoirs. *Society of Petroleum Engineers.* **2012**, SPE-162386-MS.
(30) Wang, J.; Xue, G.; Tian, B.; Li, S.; Chen, K.; Wang, D.; Sun, Y.; et al. ; Interaction between surfactants and SiO$_2$ nanoparticles in multiphase foam and its plugging ability. *Energy Fuels* **2017**, *31*, 408−417.
(31) Zeng, S.; Zhang, X.; Bai, L.; Zhang, X.; Wang, H.; Wang, J.; Bao, D.; Li, M.; Liu, X.; Zhang, S. Ionic-Liquid-Based CO$_2$ Capture Systems: Structure, Interaction and Process. *Chem. Rev.* **2017**, *117*, 9625−9673.
(32) Hosseini, H.; Dornbusch, D. A.; Suppes, G. J. Improved Electrochemical Performance of Alkaline Batteries Using Quaternary

DOI: 10.1021/acs.iecr.9b01390
Ind. Eng. Chem. Res. 2019, 58, 9431−9449

Ammonia Polysulfone-Functionalized Separators. *Ind. Eng. Chem. Res.* **2016**, *55*, 8557−8566.
(33) Chen, M.; Shafer-Peltier, K.; Randtke, S. J.; Peltier, E. Competitive association of cations with poly(sodium 4-styrenesulfonate) (PSS) and heavy metal removal from water by PSS-assisted ultrafiltration. *Chem. Eng. J.* **2018**, *344*, 155−164.
(34) Veisi, M.; Johnson, S.; Shafer-Peltier, K.; Liang, J. T.; Berkland, C.; Chen, M.; Barati, R. Controlled release of poly(vinyl sulfonate) scale inhibitor to extend reservoir treatment lifetime. *J. Appl. Polym. Sci.* **2019**, *136* (12), 47225 1−11 .
(35) Anandan, R.; Johnson, S.; Barati, R. Polyelectrolyte Complex Stabilized CO_2 Foam Systems for Hydraulic Fracturing Application. *Society of Petroleum Engineers.* **2017**, SPE-187489-MS.
(36) Nazari, N.; Tsau, J. S.; Barati, R. CO_2 Foam Stability Improvement Using Polyelectrolyte Complex Nanoparticles Prepared in Produced Water. *Energies* **2017**, *10* (4), 516.
(37) Kalyanaraman, N.; Arnold, C.; Gupta, A.; Tsau, J. S.; Ghahfarokhi, R. B. Stability improvement of CO_2 foam for enhanced oil-recovery applications using polyelectrolytes and polyelectrolyte complex nanoparticles. *J. Appl. Polym. Sci.* **2017**, *134*, 1−15.
(38) Veisi, M.; Johnson, S.; Peltier, K.; Berkland, C.; Liang, J. T.; Barati, R. Application of polyelectrolyte complex nanoparticles to increase the lifetime of poly vinyl sulfonate scale inhibitor. *Society of Petroleum Engineers.* **2018**, SPE-189564-MS.
(39) Tewes, F.; Krafft, M. P.; Boury, F. Dynamical and Rheological Properties of Fluorinated Surfactant Films Adsorbed at the Pressurized CO_2-H_2O Interface. *Langmuir* **2011**, *27*, 8144−8152.
(40) Schramm, L. L. *Foams: Fundamentals and Applications in the Petroleum Industry*; American Chemical Society: Washington, DC, 1994.
(41) Shafer-Peltier, K. E.; Haka, A. S.; Fitzmaurice, M.; Crowe, J.; Myles, J.; Dasari, R. R.; Feld, M. S. Raman microspectroscopic model of human breast tissue: Implications for breast cancer diagnosis in vivo. *J. Raman Spectrosc.* **2002**, *33*, 552−563.
(42) Howard, G. C.; Fast, C. R. Optimum Fluid Characteristics for Fracture Extension. *Society of Petroleum Engineers.* **1957**, API-57-261.
(43) CARBO Ceramics Inc. CARBOECONOPROP low density ceramic proppant. https://www.carboceramics.com/Oil-gas/Fracture-technologies/ceramic-proppant/carboeconoprop-low-density (accessed May 6, 2019).
(44) Whitfill, D. Lost Circulation Material Selection, Particle Size Distribution and Fracture Modeling with Fracture Simulation Software. *Society of Petroleum Engineers.* **2008**, SPE-115039-MS.
(45) Mahajan, S. *Encyclopedia of Materials Science and Technology*; Pergamon; U.K., 2001.
(46) Hosseini, H.; Tsau, J. S.; Peltier, E.; Ghahfarokhi, R. B. Highly stable $scCO_2$-high salinity brine interface for waterless fracturing using polyelectrolyte complex nanoparticles *Abstr. Pap. Am. Chem. Soc.* 2018, 256; Boston, MA.
(47) Agista, M. N.; Guo, K.; Yu, Z. A State-of-the-Art Review of Nanoparticles Application in Petroleum with a Focus on Enhanced Oil Recovery. *Appl. Sci.* **2018**, *8* (6), 871.
(48) Denkov, N. D.; Ivanov, I. B.; Kralchevsky, P. A.; Wasan, D. T. A possible mechanism of stabilization of emulsions by solid particles. *J. Colloid Interface Sci.* **1992**, *150* (2), 589−593.
(49) Zhang, X. L.; Penfold, J.; Thomas, R. K.; Tucker, I. M.; Petkov, J. T.; Bent, J.; Cox, A.; Campbell, R. A. Adsorption behavior of hydrophobin and hydrophobin/surfactant mixtures at the air-water interface. *Langmuir* **2011**, *27* (18), 11316−11323.
(50) Al-Anssari, S.; Barifcani, A.; Keshavarz, A.; Iglauer, S. Impact of nanoparticles on the CO_2-brine interfacial tension at high pressure and temperature. *J. Colloid Interface Sci.* **2018**, *532*, 136−142.
(51) Lau, H. C.; O'Brien, S. M. Effects of spreading and nonspreading oils on foam propagation through porous media. *SPE Reservoir Eng.* **1988**, *3*, 893−896.
(52) Kuhlman, M. Visualizing the Effect of Light Oil in CO_2 Foams. *JPT, J. Pet. Technol.* **1990**, *42* (7), 902−908.
(53) Xiao, S.; Zeng, Y.; Vavra, E. D.; He, P.; Puerto, M.; Hirasaki, G. J.; Biswal, S. L. Destabilization, Propagation, and Generation of Surfactant- Stabilized Foam during Crude Oil Displacement in Heterogeneous Model Porous Media. *Langmuir* **2018**, *34*, 739−749.
(54) Ross, S. Inhibition of Foaming. II. A Mechanism for the Rupture of Liquid Films by Antifoaming Agents. *J. Phys. Colloid Chem.* **1950**, *54* (3), 429−436.
(55) Faroughi, S. A.; Pruvot, A. J. C. J.; McAndrew, J. The rheological behavior of energized fluids and foams with application to hydraulic fracturing: Review. *J. Pet. Sci. Eng.* **2018**, *163*, 243−63.
(56) Xiao, C.; Balasubramanian, S. N.; Clapp, L. W. Rheology of Viscous CO_2 Foams Stabilized by Nanoparticles under High Pressure. *Ind. Eng. Chem. Res.* **2017**, *56*, 8340−8348.
(57) Alzobaidi, S.; Lotfollahi, M.; Kim, I.; Johnston, K. P.; Dicarlo, D. A. Carbon Dioxide-in-Brine Foams at High Temperatures and Extreme Salinities Stabilized with Silica Nanoparticles. *Energy Fuels* **2017**, *31*, 10680−10690.
(58) Stevenson, P. *Foam Engineering: Fundamentals and Applications*; Wiley: UK, 2012.
(59) Denkov, N. D.; Tcholakova, S.; Golemanov, K.; Ananthpadmanabhan, K. P.; Lips, A. The role of surfactant type and bubble surface mobility in foam rheology. *Soft Matter* **2009**, *5*, 3389−3408.
(60) Wanniarachchi, W. A. M.; Ranjith, P. G.; Perera, M. S. A.; Lashin, A.; Al Arifi, N.; Li, J. C. Current opinions on foam-based hydro-fracturing in deep geological reservoirs. *Geomech Geophys Geo-Energy Geo-Resources.* **2015**, *1*, 121−134.
(61) Zhang, J. *Chemical Engineering III*; CRC Press: London, 2014.
(62) Lauridsen, J.; Twardos, M.; Dennin, M. Shear-Induced Stress Relaxation in a Two-Dimensional Wet Foam. *Phys. Rev. Lett.* **2002**, *89*, 1−4.
(63) Szabries, M.; Jaeger, P.; Amro, M. M. Foam Analysis at Elevated Pressures for Enhanced Oil Recovery Applications *Energy Fuels* **2019**. DOI: 10.1021/acs.energyfuels.8b03088
(64) Dlugogorski, B. Z.; Schaefer, T. H.; Kennedy, E. M. Verifying Consistency of Effective-Viscosity and Pressure- Loss Data for Designing Foam Proportioning Systems. *Natl. Inst Stand Technol.* **2005**, *3*, 1−13.
(65) Boury, F.; Ivanova, T.; Panaieotov, I.; Proust, J. E.; Bois, A.; Richou, J. Dilatational Properties of Adsorbed Poly(D, L-lactide) and Bovine Serum Albumin Monolayers at the Dichloromethane/Water Interface. *Langmuir* **1995**, *11*, 1636−1644.
(66) Georgieva, D.; Cagna, A.; Langevin, D. Link between surface elasticity and foam stability. *Soft Matter* **2009**, *5*, 2063−2071.
(67) Sambasivam, A.; Sangwai, A. V.; Sureshkumar, R. Self-Assembly of Nanoparticle-Surfactant Complexes with Rodlike Micelles: A Molecular Dynamics Study. *Langmuir* **2016**, *32*, 1214−1219.
(68) Socrates, G. *Infrared and Raman characteristic group frequencies: Tables and charts*, 3rd ed.; John Wiley and Sons: UK, 2004.
(69) *Raman data and analysis.*; HORIBA JOBIN YVON Inc.; http://www.horiba.com/fileadmin/uploads/Scientific/Documents/Raman/bands.pdf (accessed May 6, 2019).
(70) Roessl, U.; Leitgeb, S.; Pieters, S.; De Beer, T.; Nidetzky, B. In situ protein secondary structure determination in ice: Raman spectroscopy-based process analytical tool for frozen storage of biopharmaceuticals. *J. Pharm. Sci.* **2014**, *103*, 2287−2295.
(71) Kumar, S.; Verma, T.; Mukherjee, R.; Ariese, F.; Somasundaram, K.; Umapathy, S. Raman and infra-red micro-spectroscopy: Towards quantitative evaluation for clinical research by ratiometric analysis. *Chem. Soc. Rev.* **2016**, *45*, 1879−900.
(72) Ben Mabrouk, K.; Kauffmann, T. H.; Aroui, H.; Fontana, M. D. Raman study of cation effect on sulfate vibration modes in solid state and in aqueous solutions. *J. Raman Spectrosc.* **2013**, *44*, 1603−1608.
(73) Wang, W.; Liu, Y.; Xue, T.; Li, J.; Chen, D.; Qi, T. Mechanism and kinetics of titanium hydrolysis in concentrated titanyl sulfate solution based on infrared and Raman spectra. *Chem. Eng. Sci.* **2015**, *134*, 196−204.
(74) Saldungaray, P.; Palisch, T. T. Hydraulic fracture optimization in unconventional reservoirs. *Society of Petroleum Engineers.* **2012**, SPE-151128-MS.

DOI: 10.1021/acs.iecr.9b01390
Ind. Eng. Chem. Res. 2019, 58, 9431−9449

(75) Harris, P. C. Dynamic Fluid-Loss Characteristics of CO_2-Foam Fracturing Fluids. *SPE Prod. Eng.* **1987**, *2*, SPE-13180-PA.
(76) Fei, Y.; Johnson, R. L., Jr.; Gonzalez, M.; Haghighi, M.; Pokalai, K. Experimental and numerical investigation into nano-stabilized foams in low permeability reservoir hydraulic fracturing applications. *Fuel* **2018**, *213*, 133−143.
(77) Ribeiro, L. H.; Sharma, M. M. Multiphase Fluid-Loss Properties and Return Permeability of Energized Fracturing Fluids. *Spe Prod Oper.* **2012**, *27* (3), 265−277.

DOI: 10.1021/acs.iecr.9b01390
Ind. Eng. Chem. Res. 2019, 58, 9431−9449